Manuscript prepared for Geoscientific Model Development (GMD)
with version 5.0 of the LaTeX class copernicus.cls.
Date: 29 September 2014

Albany/FELIX: a parallel, scalable and robust, finite element, first-order Stokes approximation ice sheet solver built for advanced analysis

Irina Kalashnikova[1], Mauro Perego[2], Andrew G. Salinger[2], Raymond S. Tuminaro[2], and Stephen F. Price[3]

[1]Quantitative Modeling and Analysis Department, Sandia National Laboratories, P.O. Box 969, MS 9159, Livermore, CA 94551, USA.
[2]Computational Mathematics Department, Sandia National Laboratories, P.O. Box 5800, MS 1320, Albuquerque, NM 87185, USA.
[3]Fluid Dynamics and Solid Mechanics Group, Los Alamos National Laboratory, P.O. Box 1663, MS B216, Los Alamos, NM, 87545, USA.

Correspondence to: Irina Kalashnikova, ikalash@sandia.gov, (248)470-9203.

Abstract. This paper describes a new parallel, scalable and robust finite-element based solver for the first-order Stokes momentum balance equations for ice flow. The solver, known as *Albany/FELIX*, is constructed using the component-based approach to building application codes, in which mature, modular libraries developed as a part of the *Trilinos* project are combined using abstract interfaces and Template-Based Generic Programming, resulting in a final code with access to dozens of algorithmic and advanced analysis capabilities. Following an overview of the relevant partial differential equations and boundary conditions, the numerical methods chosen to discretize the ice flow equations are described, along with their implementation. The results of several verification studies of the model accuracy are presented using: (1) new test cases derived using the method of manufactured solutions, and (2) canonical ice sheet modeling benchmarks. Model accuracy and convergence with respect to mesh resolution is then studied on problems involving a realistic Greenland ice sheet geometry discretized using structured and unstructured meshes. Also explored as a part of this study is the effect of vertical mesh resolution on the solution accuracy and solver performance. The robustness and scalability of our solver on these problems is demonstrated. Lastly, we show that good scalability can be achieved by preconditioning the iterative linear solver using a new algebraic multilevel preconditioner, constructed based on the idea of semi-coarsening.

1 Introduction

In its fourth assessment report (AR4), the Intergovernmental Panel on Climate Change (IPCC) declined to include estimates of future sea-level rise from ice sheet dynamics due to the inability of

ice sheet models to mimic or explain observed dynamic behaviors, such as the acceleration and thinning then occurring on several of Greenland's large outlet glaciers (IPCC, 2007). Since the AR4, increased support from United States, United Kingdom, and European Union funding agencies has enabled concerted efforts towards improving the representation of ice dynamics in ice sheet models and towards their coupling to other components of Earth System Models (ESMs) (Little et al., 2007; Lipscomb et al., 2008; van der Veen et al., 2010). Thanks to this support, there has recently been tremendous progress in the development of "next generation" community-supported ice sheet models (Bueler and Brown, 2009; Rutt et al., 2009; Larour et al., 2012b; Gagliardini et al., 2013; Brinkerhoff and Johnson, 2013; Lipscomb et al., 2013) able to perform realistic, high-resolution, continental scale simulations. These models run on high-performance, massively parallel computer (HPC) architectures using 10^2-10^4 processes and employ modern, well-supported solver libraries (e.g., *PETSC* (Balay et al., 2008) and *Trilinos* (Heroux et al., 2005)). A primary development focus has been on improving the representation of the momentum balance equations over the "shallow ice" (SIA; (Hutter, 1983)) and "shallow-shelf" (SSA; (Morland, 1987)) approximations through the inclusion of membrane stresses over the entire model domain. These approaches include "hybrid" models (a combination of SIA and SSA (Bueler and Brown, 2009; Pollard and Deconto, 2009; Goldberg and Sergienko, 2011)), so-called "higher-order" models (Pattyn, 2003), "full" Stokes models (Larour et al., 2012b; Leng et al., 2012a; Gagliardini et al., 2013)), and combinations of a range of approximations up to and including full Stokes (Seroussi et al., 2012). By accounting for both vertical and horizontal stress gradients, the aforementioned models allow for more realistic and accurate simulations of outlet glaciers, ice streams, and ice shelves, as well as modeling of the transfer of perturbations from marginal to inland regions.

Other significant improvements in ice sheet modeling frameworks include the integration of unstructured (Larour et al., 2012b; Gagliardini et al., 2013; Brinkerhoff and Johnson, 2013) or adaptive meshes (Cornford et al., 2013), which allows the focusing of resolution and computational power in regions of dynamic complexity. Also becoming standard is the use of formal optimization and data assimilation techniques for generating realistic model initial conditions. Surface observations are used to infer poorly known ice properties or parameters, such as the friction coefficient at the ice-bedrock interface (Morlighem et al., 2010; Larour et al., 2012b; Gille-Chaulet et al., 2012; Brinkerhoff and Johnson, 2013) or the rheology of floating ice shelves (Khazendar et al., 2009), allowing for a quantifiably "optimal" match between modeled and observed velocities. Recently, these approaches have been extended to simultaneously optimize both model parameter fields and uncertain initial condition fields, while also accounting for forcing from climate models in order to minimize transient shocks when coupling to climate forcing (Perego et al., 2014). Other recent and noteworthy optimization improvements include the assimilation of time dependent observations (e.g., (Goldberg and Heimbach, 2013)) and the estimation of formal uncertainties for optimized parameter fields (Petra et al., 2014).

The latter capability – the characterization of parameter uncertainties – represents a critical first step towards formal uncertainty quantification ("UQ") of ice sheet model output quantities of interests, such as estimates of future sea-level rise. For this process to be computationally tractable during both the inverse (parameter estimation and uncertainty assignment) and forward propagation steps, it is critical to have robust, efficient, and scalable solves on HPC computing platforms (Isaac et al., 2014). This, in turn, requires advanced dynamical core capabilities, such as access to model derivatives (e.g., the Jacobian matrix), and advanced algorithms for the solution of the nonlinear and linear equations. These same requirements of robustness, efficiency, and scalability hold for the inclusion of ice sheet models as fully coupled components of large-scale, high-resolution ESMs.

In this paper, we introduce a new momentum balance solver for land ice simulations based on the first-order approximation of the nonlinear Stokes flow model for glaciers and ice sheets. This new solver, *Albany/FELIX* (Finite Elements for Land Ice eXperiments, described in more detail below), either already includes many of the capabilities discussed above or is designed to allow for their easy implementation at later stages of development. Here we will present algorithms and software that lead to a robust nonlinear solution procedure (including the use of automatic differentiation (AD) technologies), scalable linear algebra, and the ability to use unstructured and highly refined grids. While we do not go into details on formal UQ and inclusion into ESMs in this paper, the same investments in AD and robust and scalable algorithms lay the groundwork for achieving these goals as well.

The remainder of this paper is organized as follows. In Section 2, we describe in detail our mathematical model for glaciers and ice sheets, giving the relevant assumptions, partial differential equations, boundary conditions, and parameter values. Our numerical methods for discretizing this model and their implementation in *Albany/FELIX* are summarized in Section 3. In Section 4, which focuses on verification of the *Albany/FELIX* code using the method of manufactured solutions, several new test cases are derived and used in a convergence verification study involving several types and orders of finite elements. In Section 5, further verification of the accuracy of solutions computed with our solver is performed using canonical ice sheet modeling test cases. The results of two mesh convergence studies on a realistic Greenland ice sheet geometry are then discussed in Section 6. These studies provide insight into the effects of the parallel domain decomposition on solver convergence. We then describe our robust, nonlinear solver, which uses homotopy continuation with respect to the regularization parameter in the calculation of the ice effective viscosity. The solver's robustness and scalability is demonstrated on various Greenland ice sheet geometries, discretized using both structured and unstructured tetrahedral and hexahedral meshes. Finally, we show that improved scalability of our code can be achieved by preconditioning the iterative linear solver using an algebraic multilevel preconditioner, constructed based on the idea of semi-coarsening. A concluding summary is offered in Section 7.

One objective of this paper is to introduce a new parallel, scalable and robust finite element first-

order Stokes solver for ice flow, namely *Albany/FELIX*, to the land ice and climate modeling communities. The article also contains several new contributions to the field of ice sheet modeling, which are most notably:

- The derivation of several new test cases based on the method of manufactured solutions for the first-order Stokes equations, which can be used to verify any ice sheet code that discretizes these equations.
- The description of a homotopy continuation algorithm with respect to a regularization parameter in the ice effective viscosity expression, which greatly improves the robustness of a Newton nonlinear solver, especially in the absence of a good initial guess.
- Insights into the effects of the parallel decomposition and vertical mesh spacing on solver performance and solution accuracy for ice sheet simulations.
- A new algebraic multilevel preconditioner, constructed based on the idea of semi-coarsening and ideal for meshes structured in the vertical direction, that delivers a scalable linear solve when combined with a preconditioned iterative method.

2 First-order Stokes approximation mathematical model

We consider a power-law viscous, incompressible fluid in a low Reynolds number flow, described by the first-order approximation to the nonlinear Stokes flow equations for glaciers and ice sheets (Dukowicz et al., 2010; Schoof et al., 2010). The first-order (FO) approximation, also referred to as the "Blatter-Pattyn" model (Pattyn, 2003; Blatter, 1995), follows from assumptions of a small geometric aspect ratio, $\delta = H/L$ (where H and L are characteristic length scales for the vertical and horizontal dimensions, respectively, and $H \ll L$), and the assumption that the normal vectors to the ice sheet's upper and lower surfaces, $\mathbf{n} \in \mathbb{R}^3$, are nearly vertical:

$$\mathbf{n}^T \approx \Big(\mathcal{O}(\delta), \mathcal{O}(\delta), \pm 1 + \mathcal{O}(\delta^2) \Big). \tag{1}$$

Effectively, the FO approximation is derived by neglecting $\mathcal{O}(\delta^2)$ terms in the Stokes equations, which are discussed in more detail in Appendix A. Numerical discretization of the FO Stokes equations gives rise to a much smaller discrete system than numerical discretization of the full Stokes equations. Moreover, discretization of the FO Stokes system gives rise to a "nice" elliptic coercive problem, in contrast to the notoriously difficult saddle-point problem obtained when discretizing the full Stokes system.

Let u and v denote the x and y components of the ice velocity vector $\mathbf{u} \equiv \Big(u, v \Big)^T \in \mathbb{R}^2$, respectively. The FO approximation consists of the following system of partial differential equations

(PDEs):

$$\begin{cases} -\nabla \cdot (2\mu \dot{\boldsymbol{\epsilon}}_1) + \rho g \frac{\partial s}{\partial x} = 0, \\ -\nabla \cdot (2\mu \dot{\boldsymbol{\epsilon}}_2) + \rho g \frac{\partial s}{\partial y} = 0, \end{cases} \tag{2}$$

where g denotes the gravitational acceleration, ρ denotes the ice density, and $s \equiv s(x, y)$ denotes the upper surface boundary:

$$\Gamma_s \equiv \{(x, y, z) \in \mathbb{R}^3 | z = s(x, y)\}. \tag{3}$$

In the most general, three-dimensional (3D) case of the FO approximation,

$$\dot{\boldsymbol{\epsilon}}_1^T = \Big(2\dot{\epsilon}_{xx} + \dot{\epsilon}_{yy},\, \dot{\epsilon}_{xy},\, \dot{\epsilon}_{xz} \Big) \in \mathbb{R}^3, \tag{4}$$

and

$$\dot{\boldsymbol{\epsilon}}_2^T = \Big(\dot{\epsilon}_{xy},\, \dot{\epsilon}_{xx} + 2\dot{\epsilon}_{yy},\, \dot{\epsilon}_{yz} \Big) \in \mathbb{R}^3, \tag{5}$$

where

$$\dot{\epsilon}_{xx} = \frac{\partial u}{\partial x}, \quad \dot{\epsilon}_{yy} = \frac{\partial v}{\partial y}, \quad \dot{\epsilon}_{xy} = \frac{1}{2}\left(\frac{\partial u}{\partial y} + \frac{\partial v}{\partial x}\right), \quad \dot{\epsilon}_{xz} = \frac{1}{2}\frac{\partial u}{\partial z}, \quad \dot{\epsilon}_{yz} = \frac{1}{2}\frac{\partial v}{\partial z}. \tag{6}$$

The effective viscosity μ can be derived using Glen's flow law (Cuffey et al., 2010; Nye, 1957) as:

$$\mu = \frac{1}{2} A^{-\frac{1}{n}} \dot{\epsilon}_e^{\frac{1}{n}-1}, \tag{7}$$

where $\dot{\epsilon}_e$ is the effective strain rate, given by:

$$\dot{\epsilon}_e^2 \equiv \dot{\epsilon}_{xx}^2 + \dot{\epsilon}_{yy}^2 + \dot{\epsilon}_{xx}\dot{\epsilon}_{yy} + \dot{\epsilon}_{xy}^2 + \dot{\epsilon}_{xz}^2 + \dot{\epsilon}_{yz}^2. \tag{8}$$

In (7), A is the flow rate factor and n is the Glen's (power) law exponent, typically taken equal to 3 for ice sheets. Hence, μ (7) is a nonlinear expression, and the system (2) is a nonlinear, elliptic system of PDEs. The flow law rate factor A is strongly temperature-dependent, and can be described through the Arrhenius relation,

$$A(T) = A_0 \exp\left(-\frac{Q}{RT}\right), \tag{9}$$

where A_0 denotes a constant of proportionality, Q denotes the activation energy for ice creep, T denotes the ice temperature in Kelvin (K), and R denotes the universal gas constant. For more details involving the relation between the flow factor and temperature (9), the reader is referred to (Cuffey et al., 2010). For completeness, the expressions for the Cauchy stress tensor $\boldsymbol{\sigma}$ and the pressure p in the FO approximation are provided:

$$\boldsymbol{\sigma} = 2\mu \Big(\dot{\boldsymbol{\epsilon}}_1,\, \dot{\boldsymbol{\epsilon}}_2,\, \mathbf{0} \Big)^T - \rho g (s - z)\mathbf{I}, \qquad p = \rho g (s - z) - 2\mu(\dot{\epsilon}_{xx} + \dot{\epsilon}_{yy}), \tag{10}$$

where $\mathbf{0} = \Big(0,\, 0,\, 0\Big)^T$ and $\mathbf{I}$ is the 3×3 identity tensor. The equations (2) are specified on a bounded 3D domain, denoted by Ω, with boundary

$$\Gamma \equiv \Gamma_s \cup \Gamma_b \cup \Gamma_l. \tag{11}$$

Here, Γ_s is the upper surface boundary (3), and

$$\Gamma_b = \{(x,y,z) \in \mathbb{R}^3 | z = b(x,y)\}, \tag{12}$$

$$\Gamma_l = \{(x,y,z) \in \mathbb{R}^3 | l(x,y) = 0\}, \tag{13}$$

are the lower and (vertical) lateral surface boundaries, respectively. The relevant boundary conditions on Γ are:

(a) A stress-free (homogeneous Neumann) boundary condition on the upper surface boundary

$$\dot{\boldsymbol{\epsilon}}_1 \cdot \mathbf{n} = \dot{\boldsymbol{\epsilon}}_2 \cdot \mathbf{n} = 0, \qquad \text{on } \Gamma_s. \tag{14}$$

(b) Either a no-slip or a sliding boundary condition on the lower surface:

$$\begin{cases} u = v = 0, & \text{on } \Gamma_0 \\ 2\mu\dot{\boldsymbol{\epsilon}}_1 \cdot \mathbf{n} + \beta u = 0, \;\; 2\mu\dot{\boldsymbol{\epsilon}}_2 \cdot \mathbf{n} + \beta v = 0, & \text{on } \Gamma_\beta, \end{cases} \tag{15}$$

where Γ_b is partitioned as $\Gamma_b = \Gamma_0 \cup \Gamma_\beta$ with $\Gamma_0 \cap \Gamma_\beta = \emptyset$, and $\beta \equiv \beta(x,y) \geq 0$ is the basal sliding coefficient. Note that we assume the partitioning of Γ_b is known *a priori*. In practice, this would be specified (through an energy balance model) by locating regions of the bed for which the temperature is at the pressure melting point. It is often more practical to enforce a quasi-no-slip Robin boundary condition on Γ_0 by setting β to a large value and always using the equation on the second line of (15) (e.g., $\beta = 10^7$ kPa a m^{-1}).

(c) On the lateral boundaries, one of two boundary conditions is applied: either a kinematic (Dirichlet) boundary condition

$$\Big\{ u = u_l, \;\; v = v_l, \text{ on } \Gamma_l, \tag{16}$$

where u_l and v_l are prescribed values of the ice velocities on the lateral boundary, or a dynamic (Neumann) boundary condition

$$\Big\{ 2\mu\dot{\boldsymbol{\epsilon}}_i \cdot \mathbf{n} - \rho g(s-z)\mathbf{n} = \rho_w g \max(z,0)\mathbf{n}, \text{ on } \Gamma_l, \tag{17}$$

for $i = 1,2$, where ρ_w denotes the density of water. In (17), it has been assumed that the coordinate system has been oriented such that z is strictly elevation (that is, $z = 0$ at sea level and values of z increase for higher elevations) (MacAyeal et al., 1996). The boundary condition (17) is derived by assuming that the ice shelf is in hydrostatic equilibrium with the

air/water that surrounds it and is often referred to as an "open-ocean" boundary condition, as it takes into account the pressure exerted on the ice shelf by neighboring ocean. For some canonical benchmark experiments performed here (see Section 5.1), periodic lateral boundary conditions are prescribed as well.

The values of the parameters that appear in the first-order Stokes equations and the boundary conditions described above and used herein are summarized in Table 1. From this point forward, the new first-order Stokes approximation momentum balance solver will be referred to "*Albany/FELIX*". In this code, the numerical discretization of (2) uses *Trilinos*, a suite of modular software libraries (described in detail in (Heroux et al., 2005)).

Table 1. Physical parameter values for first-order Stokes equations and boundary conditions*

Name	Value	Units	Description
A	10^{-4}	$\mathrm{k}^{-(n+1)}\ \mathrm{Pa}^{-n}\ \mathrm{a}^{-1}$	Flow rate factor
n	3	–	Glen's flow law exponent
g	9.8	$\mathrm{m\ s}^{-2}$	Gravitational constant
ρ	910	$\mathrm{kg\ m}^{-3}$	Ice density
ρ_w	1025	$\mathrm{kg\ m}^{-3}$	Ocean water density
R	8.314	$\mathrm{J\ K}^{-1}\ \mathrm{mol}^{-1}$	Universal gas constant
A_0	$\begin{cases} 1.30 \times 10^7, & \text{if } T < 263 \text{ K}, \\ 6.22 \times 10^{22}, & \text{if } T \geq 263 \text{ K} \end{cases}$	$\mathrm{k}^{-(n+1)}\ \mathrm{Pa}^{-n}\ \mathrm{s}^{-1}$	Arrhenius constant of proportionality
Q	$\begin{cases} 6.00 \times 10^4, & \text{if } T < 263 \text{ K}, \\ 1.39 \times 10^5, & \text{if } T \geq 263 \text{ K}, \end{cases}$	$\mathrm{J\ mol}^{-1}$	Activation energy for ice creep

*The symbol k in the table denotes km/m, i.e., k=km/m= 10^3.

3 Numerical discretization and implementation

The model described in Section 2 is discretized and solved using a collection of algorithms and software implementations that were selected for accuracy, flexibility, robustness, and scalability. The following brief discussion of the methods presumes prior knowledge of Galerkin finite element approaches and Newton-Krylov based nonlinear solvers (Strang and Fix, 1973; Pawlowski et al., 2006).

3.1 Numerical methods

The PDEs for the FO Stokes model defined by (2) and the associated boundary conditions are discretized using the classical Galerkin finite element method (FEM) (Hughes, 2000).

Let $\mathcal{V}$ denote the Hilbert space given by:

$$\mathcal{V} \equiv \mathcal{V}(\Omega) = \left\{ \phi \in H^1(\Omega) : \phi|_{\Gamma_0} = 0 \right\}, \tag{18}$$

where $H^1(\Omega)$ denotes the space of square-integrable functions whose first derivatives are also square integrable. Following classical Galerkin FEM methodology, the weak form of the problem is obtained by projecting each of the equations in (2) onto a test function in $\mathcal{V}$ (18) in the continuous L^2 inner product and integrating the second order terms by parts. Toward this effect, the weak formulation of (2) reads: find $u, v \in \mathcal{V}$ such that

$$\begin{cases} \int_\Omega 2\mu\dot{\boldsymbol{\epsilon}}_1(u,v) \cdot \nabla\phi_1 d\Omega + \int_{\Gamma_\beta} \beta u \phi_1 d\Gamma + \int_\Omega \rho g \frac{\partial s}{\partial x} \phi_1 d\Omega = 0, \\ \int_\Omega 2\mu\dot{\boldsymbol{\epsilon}}_2(u,v) \cdot \nabla\phi_2 d\Omega + \int_{\Gamma_\beta} \beta v \phi_2 d\Gamma + \int_\Omega \rho g \frac{\partial s}{\partial y} \phi_2 d\Omega = 0, \end{cases} \tag{19}$$

for all $\phi_1, \phi_2 \in \mathcal{V}(\Omega)$. The surface integral along the boundary appearing in (19) arises from integrating the stress term in the variational form of the PDEs by parts. This approach leads to a weak enforcement of the basal surface boundary condition (15) for the tangential stress, and straightforward implementation of the basal boundary conditions as an integrated boundary condition. (We believe, but have not rigorously shown, that the Gelerkin finite element approach for implementing the basal surface boundary condition enables one to circumvent robustness issues stemming from the discretization that were previously seen in our work with a finite difference discretization (Lemieux, 2011).) Note that in our weak formulation (19), the source terms in (2) have not been integrated by parts.

Letting $\mathcal{F}(u, v; \phi_1, \phi_2)$ denote the operator defining the left hand side of (19), the problem defined by (19) is equivalent to finding the roots $u, v \in \mathcal{V}$ of the following nonlinear equation:

$$\mathcal{F}(u, v; \phi_1, \phi_2) = 0, \qquad \forall \phi_1, \phi_2 \in \mathcal{V}. \tag{20}$$

Equation (20) is an infinite-dimensional problem; a finite-dimensional analog of (20) is obtained by replacing the infinite-dimensional space $\mathcal{V}$ by a finite-dimensional finite element space, $\mathcal{V}_h$, where h is a length scale associated with a triangulation of the domain Ω into a set of disjoint finite elements Ω_e ($\Omega = \cup_{e=1}^{n_{el}} \Omega_e$, where $n_{el} \in \mathbb{N}$ is the number of finite elements in the triangulation).

Our implementation (a detailed discussion of which is given in Section 3.2) allows for tetrahedral (with either trilinear or triquadratic basis functions) or hexahedral elements (with bilinear or biquadratic basis functions) for 3D problems. One reason a finite element approach was selected was for its flexibility in using unstructured grids with non-uniform mesh density to increase the resolution in areas of large velocity gradients, such as in the vicinity of outlet glaciers, while retaining relatively coarse meshes in the more static interior regions. In this paper, we present results on three different types of grids:

(i) Structured uniform hexahedral grids,

(ii) Structured uniform tetrahedral grids,

(iii) Unstructured non-uniform tetrahedral grids.

The structured hexahedral meshes are generated by creating a uniform quadrilateral grid of a two-dimensional (2D) horizonal cross-section of a geometry Ω, and extruding it in a uniform fashion as hexahedra in the vertical direction. Similarly, the structured tetrahedral meshes are created by meshing a 2D horizonal cross-section of Ω using a uniform triangular mesh, extruding it in the vertical direction as prisms, then splitting each prism into three tetrahedra (Figure 17). For the unstructured tetrahedral grids, an unstructured Delaunay triangle mesh of a 2D cross-section of Ω is generated based on some kind of refinement criteria (e.g., a static refinement based on the gradient of the velocity) using a meshing software (e.g., *Triangle*, a Delaunay triangulation mesh (Shewchuk et al., 1996)), and extruded in the vertical direction in the same way as a structured triangular grid. More details on these meshes are provided in Sections 5 and 6. Note that although all the meshes employed for the ice sheet application considered here were extruded (structured) in the vertical direction, our code base allows for completely unstructured grids.

A domain decomposition approach is used to compute the solution to the discretized nonlinear problem on distributed memory parallel computers. As a pre-processing step, the elements of the mesh are partitioned into one contiguous domain per processor to provide nearly equal work per processor.

The result of the discretization process is a large, sparse system of nonlinear algebraic equations for the two components of horizontal velocity at the nodes of the mesh (the discrete counterpart of (20)). Our approach to solving this fully-coupled, nonlinear system is Newton's method. An analytic Jacobian matrix is computed at each iteration of Newton's method using automatic differentiation (AD). The integration of AD into the Albany code base, both for Jacobians and for parameter derivatives for sensitivity analysis and UQ, has been a significant advantage of developing a new model in this framework. The matrix is stored in sparse form, with rows of the matrix distributed across the processors of the machine.

The resulting linear system is solved using a preconditioned iterative method. For the largest problems, we use multilevel preconditioning (described in Section 3.1.2) to achieve scalability, while incomplete LU (ILU) additive Schwartz preconditioners work well for modest problem sizes and processor counts. Since the model is symmetric, the Conjugate Gradient (CG) iterative linear solver is employed.

Because of the singularity in the viscosity formulation for stress-free solutions, such as when computing the nonlinear solution from a trivial initial guess, the Newton iteration does not reliably converge. To achieve a robust nonlinear solution procedure, we formulated and implemented a homotopy continuation approach that steps to the final solution by solving a series of nonlinear problems that reliably converge. The details of this algorithm are given in Section 3.1.1.

3.1.1 Homotopy continuation algorithm

Although the stress tensor $\boldsymbol{\sigma}$ (10) is well-defined for any differentiable function $\mathbf{u}$, the Glen's law effective viscosity (7) is not defined when $\mathbf{u}$ is a rigid movement or exactly 0 (because n is typically taken to be greater than 1; see e.g., (Schoof, 2010; Chen et al., 2013)). This can pose a problem for nonlinear solvers as the initial guess for $\mathbf{u}$ is often taken as uniform or 0. To circumvent this difficulty, a regularization parameter $\gamma > 0$, $\gamma \ll 1$ is added to the sum of the strain rates in the effective strain rate term of the effective viscosity (7), yielding what we refer to as μ_γ:

$$\mu_\gamma = \frac{1}{2} A^{-\frac{1}{n}} \left(\dot{\epsilon}_e^2 + \gamma\right)^{\left(\frac{1}{2n} - \frac{1}{2}\right)}, \qquad \text{where } \lim_{\gamma \to 0} \mu_\gamma = \mu. \tag{21}$$

One common practice is to define $\mu = \mu_\gamma$ in (7) using some small, fixed value for γ, e.g., $\gamma = 10^{-10}$. Here, noting that the nonlinear solver often struggles to converge initially when using Newton's method, we use a variable γ as the continuation parameter in a homotopy method (Algorithm 1). In this approach, a sequence of problems (2) is solved for a sequence of effective viscosities $\{\mu_{\gamma_i}\}$ for $i = 1, 2, ...$, with $0 < \gamma_{i+1} < \gamma_i$, until γ reaches its target value. We use a natural continuation procedure, where the final solution at one value of the continuation parameter α is used as the initial guess for the subsequent nonlinear problem. The continuation algorithm has adaptive step size control, and will backtrack and attempt a smaller parameter step if the nonlinear solve at some step fails to converge (Allgower et al., 2003). We have found that starting with $\alpha_0 = 0$ leads to a system that will reliably converge from a trivial initial guess, and that $\alpha_\infty = 1$ provides an adequate stopping value.

Algorithm 1 Homotopy continuation on regularization parameter γ in μ_γ

Set $\alpha = \alpha_0$, $\mathbf{u}^0 = \mathbf{u}_0$ and $i = 0$.
while $\alpha \leq \alpha_\infty$ **do**
  Set $\gamma = 10^{-10\alpha}$ and define μ_γ by the formula (21).
  Set $\mu = \mu_\gamma$ in (7).
  Set $i = i + 1$.
  Solve (2) with initial guess $\mathbf{u}^{i-1}$ using Newton's method, to obtain $\mathbf{u}^i$.
  Increase α using a homotopy continuation method (e.g., natural continuation).
end while

In general, the homotopy continuation approach leads to many fewer nonlinear solves than when the regularization parameter γ in (21) is fixed to some small value, e.g., $\gamma = 10^{-10}$, especially for problems where a "good" initial guess for Newton's method is unavailable. Moreover, with the homotopy continuation approach, it is found that a full step can often be employed in the Newton's method line search algorithm, without the need for backtracking (i.e., iteratively reducing the step size in the line search algorithm).

We note that the homotopy continuation approach is in general effective when the initial guess

is *not* close to the solution (in which case μ_γ is very small). Similarly, a good initial guess for $\mathbf{u}$ may not be a good initial guess when using continuation because the initial viscosity μ_{γ_0} for the continuation algorithm is generally far from the real viscosity μ. When solving transient problems, it may be better to simply use a standard Newton method (without homotopy continuation), taking the solution at the previous time step as the initial guess, and using homotopy continuation only if the Newton solver has difficulties converging. A different approach, which may be used as an alternative to homotopy continuation, is to perform a few iterations using the Picard method and then switch to the Newton method once the nonlinear iterations starts to converge (e.g., (Leng et al., 2014)). The robustness and efficiency of the Newton solver with the homotopy continuation approach summarized in Algorithm 1 is studied numerically in Section 6.3.1.

3.1.2 Multilevel preconditioning

Multigrid preconditioners are among the most efficient and scalable linear solution techniques for resolving matrix equations associated with elliptic operators. The basic idea is to capture errors by utilizing multiple resolutions. Oscillatory components are effectively reduced through a simple iterative procedure, while smooth components are tackled using auxiliary lower resolution versions of the problem. Different geometric multigrid methods have been successfully applied to the linear systems arising from ice sheet modeling simulations (Brown et al., 2013; Cornford et al., 2013).

For our capability, we prefer algebraic multigrid (AMG) methods due to the potentially unstructured nature of the mesh in the horizontal plane. AMG methods have the advantage that the lower resolution versions of the multigrid hierarchy are constructed automatically using only the matrix coefficient entries. Unfortunately, solution of the underlying linear systems is problematic due to the strong anisotropic nature of the discrete equations. This is essentially a consequence of the disparate scales in the horizontal and vertical directions and the associated large mesh aspect ratios. At the discrete level, these aspect ratios give rise to matrices where entries representing vertical coupling are generally much larger than entries representing horizontal coupling. Anisotropic phenomena within ice sheets and fairly different types of multigrid methods have been considered in recent prior works (Brown et al., 2013; Isaac et al., 2014).

From a multigrid perspective, reducing oscillatory errors in the horizontal direction is much more difficult than in the vertical direction. Further, accurately capturing horizontal coupling on coarse levels can be challenging due to the relatively small size of the corresponding matrix entries (which are effectively averaged to generate the low resolution versions). To avoid these difficulties, we have developed a hybrid structure/unstructured AMG multigrid capability that leverages the fact that our meshes, though unstructured in the horizontal plane, are structured in the vertical direction. That is, our 3D meshes can be viewed as extrusions of unstructured 2D meshes, allowing for varying vertical mesh spacing. A paper is in preparation to further describe the details of this hybrid algorithm. Here, we briefly describe its essence.

The basic concept behind the hybrid structured/unstructured AMG method is to first apply operator dependent multigrid semi-coarsening to initially coarsen the mesh and construct the first few levels of the multigrid hierarchy. Semi-coarsening and operator dependent multigrid both have a long history on structured grid problems (Dendy et al., 2010; Schaffer, 1998; Brown et al., 2000). Semi-coarsening refers to only coarsening in some subset of coordinate directions and is often advocated to address anisotropic problems. Essentially, one only coarsens in directions where oscillatory errors are easily reduced. Operator dependent multigrid refers to family of algorithms that intimately take advantage of structure. They can be viewed as idealized or "perfect" grid transfers for one dimensional simplifications of the higher dimensional problem. In this way, several coarse level meshes are effectively constructed, each containing the same number of points within all horizontal planes. When it is no longer possible to further coarsen vertically (as there is just a single horizontal layer), a standard smoothed aggregation AMG method is applied to this horizontal problem creating additional levels in the hierarchy. Thus, finer levels of the hierarchy are created via semi-coarsening and operator dependent multigrid (leveraging grid structure). Coarser levels are constructed via AMG, which is applied after the anisotropic behavior is no longer present (as there is just a single horizontal layer). To complete this brief description, we note that line Jacobi is used as the simple iterative scheme to damp oscillatory errors on the finer levels. It allows for aggressive semicoarsening (i.e., reduction factors greater than three in the linear system dimension as one proceeds to progressively coarser levels). Polynomial smoothing is used on the levels associated with standard AMG.

The algebraic multilevel preconditioner described above has been implemented in and is available through the (open-source) *ML* package of *Trilinos* (Heroux et al., 2005).

3.2 Software implementation

The numerical methods described above are implemented in the *Albany* code base, an open-source[1], multi-physics code/analysis package developed at Sandia National Laboratories. A full description of *Albany* can be found in a separate publication (Salinger et al., 2014). Briefly, *Albany* is a finite element code base for the solution and analysis of models of coupled PDEs using parallel, unstructured-grid, implicit algorithms. It makes use of numerous computational mathematics libraries from the *Trilinos* suite (Heroux et al., 2005), and has been previously used in other applications domains such as quantum device modeling (Gao et al., 2013) and computational mechanics (Sun et al., 2013).

The software stack in *Albany* involves dozens of libraries that are delivered through *Trilinos* as independent software packages developed by small teams of domain experts. The *Sierra ToolKit* (*STK*) package is used for mesh database structures and mesh I/O. The *Epetra* package is used for distributed memory, parallel data structures for vectors and sparse matrices, which greatly simplify parallel operations such as halo exchanges for synchronizing data between processors. The *Intrepid*

[1]The *Albany* code can be obtained from its public `github` repository by the interested reader: https://github.com/gahansen/Albany.

(Bochev et al., 2012) package provides flexible finite element discretization algorithms and general integration kernels. The PDE equations are described by a set of evaluation kernels, whose evaluation is managed by the *Phalanx* package.

One of the main distinguishing characteristics of the *Albany* code base is the use of the Template-Based Generic Programming (TBGP) approach (Pawlowski et al., 2012a,b). With this methodology, all that is required to implement a new set of physics in *Albany* is to code the residual of the PDE equations. Given this residual, *Albany* automatically computes and assembles the sparse Jacobian matrix and sensitivity vectors without any additional code development. TBGP makes extensive use of the *Sacado* package (Phipps et al., 2012) for automatic differentiation, which employs C++ expression templates with operator overloading, and has been closely integrated with the *Phalanx* and *Intrepid* packages.

The Newton-based nonlinear system solver and homotopy continuation algorithm are implemented in the *NOX* (Pawlowski et al., 2006) and *LOCA* (Salinger et al., 2005) packages, respectively. These solvers can additionally perform sensitivity analysis using the analytic sensitivity vectors computed with automatic differentiation with respect to model parameters. Within the solvers, we have full runtime access to all the *Trilinos* preconditioners (ILU and algebraic multilevel preconditioners, from the *Ifpack* and *ML* software packages, respectively) and linear solvers by specification in an input file. For the bulk of the computations in this paper, the *ML* package was employed for algebraic multilevel preconditioners (Tuminaro, 2014), and the *Belos* package was employed for CG-based iterative solvers (Bavier et al., 2012).

Albany is also coupled to the *Dakota* framework (Adams et al., 2013) of sampling-based optimization and UQ algorithms, which will play a significant role in model initialization, calibration, and projections. Although the application of optimization and UQ algorithms go beyond the scope of this paper, we emphasize that the component-based approach for building this application code leads to the rapid incorporation of many sophisticated capabilities.

4 Verification using the method of manufactured solutions (MMS)

We first conduct formal verification of the new *Albany/FELIX* code described in Section 3 through the method of manufactured solutions (MMS), using test cases derived here explicitly for this purpose. A survey of the literature reveals that past work has focused on deriving MMS benchmarks for the "shallow ice" and nonlinear Stokes models (e.g., (Bueler et al., 2007), (Leng et al., 2012b), respectively) rather than the FO approximation (2), and the derivation of MMS benchmarks for the FO approximation is one of the novel contributions of this paper. Here, we use the *Albany/FELIX* code and these new MMS benchmarks to verify (i) that the dynamics have been implemented correctly, and (ii) that the type of finite elements employed show convergence at their expected theoretical rates.

Consider the FO Stokes equations (2) in 2D on a rectangular geometry with domain edges aligned with the $x-$ and $y-$ axes in a Cartesian reference frame, $\Omega = (0,1) \times (0,1) \in \mathbb{R}^2$, and $\frac{\partial s}{\partial x} = \frac{\partial s}{\partial y} = 0$. Let $\mathbf{f}^T \equiv \Big(f_1,\, f_2 \Big)$ be a source term for the equations (2), to be determined such that a given manufactured solution satisfies these equations. Under these assumptions, the FO Stokes system (2) has the following form:

$$\begin{cases} -\frac{\partial}{\partial x}\left(4\mu_{2D}\frac{\partial u}{\partial x} + 2\mu_{2D}\frac{\partial v}{\partial y}\right) - \frac{\partial}{\partial y}\left(\mu\frac{\partial u}{\partial y} + \mu_{2D}\frac{\partial v}{\partial x}\right) + f_1 = 0, \\ -\frac{\partial}{\partial x}\left(\mu_{2D}\frac{\partial u}{\partial x} + \mu_{2D}\frac{\partial v}{\partial y}\right) - \frac{\partial}{\partial y}\left(2\mu_{2D}\frac{\partial u}{\partial x} + 4\mu_{2D}\frac{\partial v}{\partial y}\right) + f_2 = 0, \end{cases} \tag{22}$$

where the viscosity μ_{2D} is given by the 2D version of (7):

$$\mu_{2D} = \frac{1}{2}A^{-\frac{1}{n}}\left(\dot{\epsilon}_{xx}^2 + \dot{\epsilon}_{yy}^2 + \dot{\epsilon}_{xx}\dot{\epsilon}_{yy} + \dot{\epsilon}_{xy}^2\right)^{\left(\frac{1}{2n} - \frac{1}{2}\right)}. \tag{23}$$

For the MMS test cases considered here, the values of the flow rate factor and Glen's flow law exponent were taken to be $A = 1$ and $n = 3$, respectively.

We consider four different finite element types in our numerical convergence study: three node triangles (denoted by "Tri 3"), four node quadrilaterals (denoted by "Quad 4"), six node triangles (denoted by "Tri 6"), and nine node quadrilaterals (denoted by "Quad 9") (Figure 1). Convergence is evaluated in the discrete l^2 norm. In particular, the relative error in a computed solution, denoted by $\mathcal{E}_{rel}^{disc}$, is calculated from

$$\mathcal{E}_{rel}^{disc} = \frac{||\mathbf{u}_n - \mathbf{u}||_2}{||\mathbf{u}||_2}, \tag{24}$$

where $||\cdot||_2$ denotes the discrete l^2 norm, $\mathbf{u}^T \equiv \Big(u,\, v \Big)$ is the exact solution to (22), and $\mathbf{u}_n$ is the numerically computed solution to (22). It is well-known from classical finite element theory (Hughes, 2000) that the theoretical convergence rate in the norm considered is two for the Tri 3 and Quad 4 elements, and three for the Quad 6 and Quad 9 elements. Hence, the first two elements are referred to as first-order finite elements and the second two elements are referred to as second-order finite elements. Note that the quadrilateral elements are expected to deliver a more accurate solution than their triangular counterparts of the same order.

4.1 Dirichlet/Neumann boundary condition test case ("sin-cos" test case)

The first MMS test case considered is referred to as the "sin-cos" test case, as the solution to this problem is a product of the sine and cosine functions. The source term in (22) is derived such that the exact solution to this system is given by the following trigonometric expression:

$$\begin{aligned} u &= \sin(2\pi x + \phi)\cos(2\pi y + \psi) + 3\pi x, \\ v &= -\cos(2\pi x + \phi)\sin(2\pi y + \psi) - 3\pi y. \end{aligned} \tag{25}$$

The parameters $\phi, \psi \in [0, 2\pi)$ in (25) are phase shifts that can be used to generate a family of solutions (e.g., Figure 2). The solution (25) satisfies a combination of Dirichlet and Neumann boundary

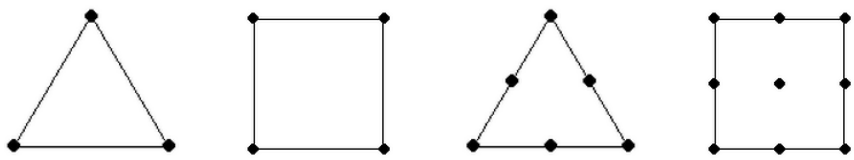

(a) (b) (c) (d)

Fig. 1. 2D finite elements evaluated in the manufactured solution test cases. (a) Tri 3, (b) Quad 4, (c) Tri 6, (d) Quad 9

conditions on the boundary of Ω, denoted by Γ. For $\phi = \psi = 0$, the boundary conditions are as follows:

$$\begin{aligned} u &= 0, \quad \dot{\boldsymbol{\epsilon}}_2 \cdot \mathbf{n} = 0, \quad \text{at } x = 0, \\ u &= 3\pi, \; \dot{\boldsymbol{\epsilon}}_2 \cdot \mathbf{n} = 0, \quad \text{at } x = 1, \\ \dot{\boldsymbol{\epsilon}}_1 \cdot \mathbf{n} = 0, \quad v &= 0, \quad \text{at } y = 0, \\ \dot{\boldsymbol{\epsilon}}_1 \cdot \mathbf{n} = 0, \quad v &= -3\pi, \text{ at } y = 1, \end{aligned} \tag{26}$$

where $\mathbf{n}$ denotes the outward unit normal vector to a given boundary.

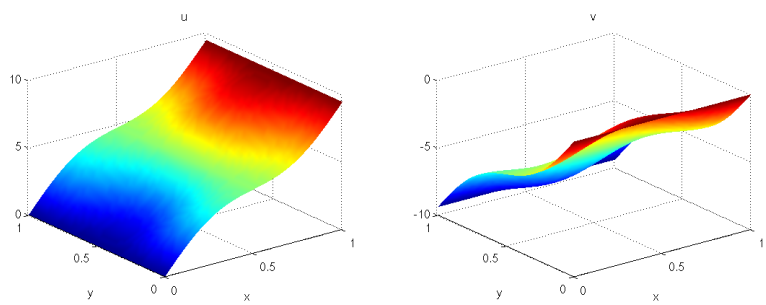

(a) (b)

Fig. 2. Plots of exact solutions to the "sin-cos" test case for $\phi = \psi = 0$: (a) u, (b) v

Substituting (25) into (22), the following expressions for the source terms f_1 and f_2 are obtained:

$$f_1 = -8\mu_{2D}\pi^2 \sin(2\pi x+\phi)\cos(2\pi y+\psi) + A^{-\frac{1}{n}}\left(\frac{1}{n}-1\right)\dot{\epsilon}_{e,2D}^{\frac{1}{n}-2}\left(\frac{\partial \dot{\epsilon}_{e,2D}}{\partial x}(2\epsilon_{xx}+\epsilon_{yy}) + \frac{\partial \dot{\epsilon}_{e,2D}}{\partial y}\epsilon_{xy}\right), \tag{27}$$

$$f_2 = 8\mu_{2D}\pi^2 \cos(2\pi x+\phi)\sin(2\pi y+\psi) + A^{-\frac{1}{n}}\left(\frac{1}{n}-1\right)\dot{\epsilon}_{e,2D}^{\frac{1}{n}-2}\left(\frac{\partial \dot{\epsilon}_{e,2D}}{\partial x}\epsilon_{xy} + \frac{\partial \dot{\epsilon}_{e,2D}}{\partial y}(\epsilon_{xx}+2\epsilon_{yy})\right),$$

(28)

where

$$\dot{\epsilon}_{e,2D} = 2\pi\cos(2\pi x + \phi)\cos(2\pi y + \psi) + 3\pi x, \tag{29}$$

is the effective strain rate in 2D (i.e., the 2D analog of (8)) and

$$\mu_{2D} = \frac{1}{2} A^{-\frac{1}{n}} \dot{\epsilon}_{e,2D}^{\frac{1}{n}-1}. \tag{30}$$

Figure 3 plots the relative error (computed according to formula (24)) in the solution to the "sin-cos" test case as a function of the mesh spacing h on a log-log plot for $\phi = \psi = 0$. The reader can observe that the two lowest-order (Tri 3 and Quad 4) finite elements converge at their theoretical convergence rates; a slight superconvergence is observed for the two higher order elements (Tri 6 and Quad 9). Moreover, the quadrilateral elements deliver a solution that is more accurate than that from their triangular counterparts, as expected.

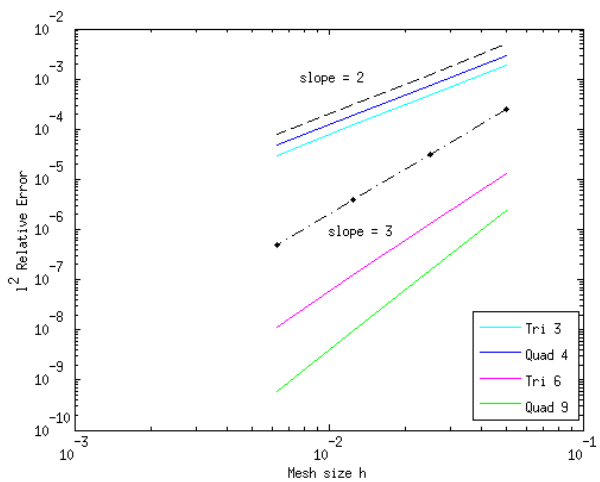

Fig. 3. Convergence rates for "sin-cos" MMS test case in the discrete l^2 norm (24)

4.2 Robin boundary condition test case ("sin-cos-exp" test case)

We refer to the second MMS test case as the "sin-cos-exp" test case, as the solution to this problem is a product of the sine or cosine function and the exponential function. This test case is posed on the same geometry as the "sin-cos" test case, namely $\Omega = (0,1) \times (0,1)$, but differs in that it has a different source term and different boundary conditions, which are of the Robin type on some boundaries of Ω. The source term in (22) is derived such that the exact solution to this system is given by the following expression:

$$\begin{aligned} u &= e^x \sin(2\pi y), \\ v &= e^x \cos(2\pi y). \end{aligned} \tag{31}$$

(Figure 4). Substituting (31) into (22), the source terms f_1 and f_2 are obtained:

$$f_1 = 2\mu_{2D} e^x \sin(2\pi y)\left[2 - 3\pi - 2\pi^2\right] + A^{-\frac{1}{n}}\left(\frac{1}{n} - 1\right)\dot{\epsilon}_{e,2D}^{\frac{1}{n}-2}\left(\frac{\partial \dot{\epsilon}_{e,2D}}{\partial x}(2\epsilon_{xx} + \epsilon_{yy}) + \frac{\partial \dot{\epsilon}_{e,2D}}{\partial y}\epsilon_{xy}\right), \tag{32}$$

$$f_2 = 2\mu_{2D} e^x \cos(2\pi y)\left[3\pi + \frac{1}{2} - 8\pi^2\right] + A^{-\frac{1}{n}}\left(\frac{1}{n} - 1\right)\dot{\epsilon}_{e,2D}^{\frac{1}{n}-2}\left(\frac{\partial \dot{\epsilon}_{e,2D}}{\partial x}\epsilon_{xy} + \frac{\partial \dot{\epsilon}_{e,2D}}{\partial y}(\epsilon_{xx} + 2\epsilon_{yy})\right), \tag{33}$$

where

$$\dot{\epsilon}_{e,2D} = e^x\sqrt{(1 + 4\pi^2 - 2\pi)\sin^2(2\pi y) + \frac{1}{4}(2\pi + 1)^2\cos^2(2\pi y)}, \tag{34}$$

is the effective strain rate in 2D, and μ_{2D} is given by (30). The solution (31) implies the following boundary conditions on the boundary of Ω:

$$\begin{aligned}
&\dot{\boldsymbol{\epsilon}}_1 \cdot \mathbf{n} = 2(\pi - 1)u, && \dot{\boldsymbol{\epsilon}}_2 \cdot \mathbf{n} = -\left(\pi + \tfrac{1}{2}\right)v, && \text{at } x = 0,\\
&\dot{\boldsymbol{\epsilon}}_1 \cdot \mathbf{n} = -2(\pi - 1)u, && \dot{\boldsymbol{\epsilon}}_2 \cdot \mathbf{n} = \left(\pi + \tfrac{1}{2}\right)v, && \text{at } x = 1,\\
&u = 0, && \dot{\epsilon}_2 \cdot \mathbf{n} = 0, && \text{at } y = 0 \text{ and } y = 1,\\
&v = 0, && && \text{at } (x, y) = (0, 0),
\end{aligned} \tag{35}$$

where $\mathbf{n}$ denotes the outward unit normal vector to a given boundary. The last condition on (35) is imposed to guarantee uniqueness of the v component of the velocity vector.

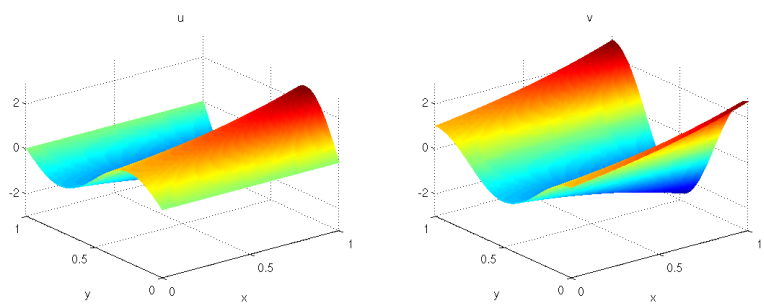

(a) (b)

Fig. 4. Plots of exact solutions to the "sin-cos-exp" test case: (a) u, (b) v

The relative errors (24) as a function of the mesh size h for the sin-cos-exp test case are plotted on a log-log plot in Figure 5. The two lowest-order finite elements (Tri 3 and Quad 4) converge at their theoretical rates of two, whereas the higher-order finite elements (Tri 6 and Quad 9) exhibit a slight superconvergece over their theoretical convergence rate of three. As expected, the quadrilateral elements deliver a more accurate solution than their triangular counterparts.

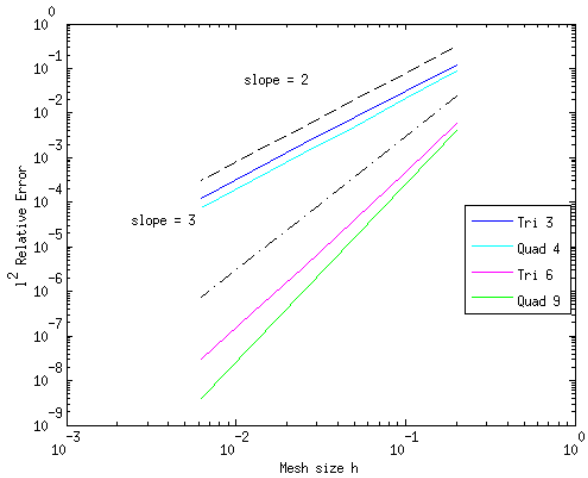

Fig. 5. Convergence rates for "sin-cos-exp" MMS test case in the discrete l^2 norm (24)

5 Intercomparison with other codes and benchmarks

In this section we discuss further (informal) verification of results for *Albany/FELIX* using some canonical ice sheet benchmarks, namely ISMIP-HOM tests A and C (Section 5.1), and the confined shelf test case (Section 5.2) (Pattyn et al., 2008). For these problems, the exact solution is not known in closed analytic form and our quasi-verification consists of code-to-code comparisons between the solution computed in *Albany/FELIX*, the results from other models participating in the original benchmark experiments, and the FO approximation, finite element code of (Perego et al., 2012).

The values of the physical parameters used in the two test cases considered are summarized in Table 1. We note that the units employed in our implementation are m a^{-1} for the ice velocities u and v (where "a" denotes years) and km for the length scale (e.g., the mesh dimensions). Our units are the same as in (Perego et al., 2012) but differ from other implementations, which often use a length scale of meters (m). Our units give rise to matrices with smaller differences in scale (which may be better scaled), as there is in general a smaller difference in scale in the relevant parameter values (e.g., $A = 10^{-4}$ k$^{-(n+1)}$ Pa^{-n} a^{-1} when the mesh is in km versus $A = 10^{-16}$ Pa^{-n} a^{-1} when the mesh is in m, where k=km/m=10^3).

5.1 ISMIP-HOM benchmarks

The ISMIP-HOM test cases (Pattyn et al., 2008) are a canonical set of benchmark experiments for so-called "higher-order" ice sheet models. Here, we consider tests A and C, both of which are specified on a horizontal, periodic domain with a unit length of L km. The bedrock surface, Γ_b, is given by a continuous function $z = b(x, y) \in \mathbb{R}^2$ and the upper surface, Γ_s, is given by a continuous function $z = s(x, y) \in \mathbb{R}^2$. The geometries are generated from a uniform hexahedral mesh of the

unit cube $(0,1)^3 \in \mathbb{R}^3$ via the following transformation:

$$x = LX, \qquad y = LY, \qquad z = s(x,y)Z + b(x,y)(1-Z), \tag{36}$$

where X, Y, Z are the coordinates of the unit cube (in km), and $L \in \mathbb{N}$ is given. That is, a uniform mesh of $n_x \times n_y \times n_z$ elements is first generated of $(0,1)^3$, to yield the nodal coordinates X, Y, and Z, then the transformation (36) is applied. The following domain sizes are considered: $L = 5, 10, 20, 40, 80$ and 160 km. Each domain is discretized using an $80 \times 80 \times 20$ mesh of hexahedral elements. As a part of the quasi-verification, the *Albany/FELIX* solution is compared with the solution computed in the finite element code of (Perego et al., 2012) at the upper surface along the line $y = L/4$. Table 2 shows the relative difference between the *Albany/FELIX* and (Perego et al., 2012) solutions in the l^2 norm along this line, calculated from the formula (24) with the (Perego et al., 2012) solution taken as the reference solution. Differences in the solutions are likely due to the different finite elements used: trilinear finite elements on hexahedra are used in *Albany/FELIX*, whereas linear finite elements on tetrahedra are used in the code of (Perego et al., 2012).

5.1.1 ISMIP-HOM test A

The first ISMIP-HOM benchmark considered is test A. For this problem, the upper ice surface boundary (Γ_s) is given by the following linear function

$$s(x,y) = -x \tan\alpha, \tag{37}$$

and the bedrock boundary (Γ_b) is given by the following trigonometric function

$$b(x,y) = s(x,y) - 1 + \frac{1}{2}\sin\left(\frac{2\pi}{L}x\right)\sin\left(\frac{2\pi}{L}y\right), \tag{38}$$

with $\alpha = 0.5°$. The geometry is thus that of a uniformly sloping slab along the x coordinate direction with a doubly periodic, "egg crate" shaped bed. A no-slip boundary condition is prescribed on Γ_b (with $\Gamma_0 \equiv \Gamma_b$ and $\Gamma_\beta = \emptyset$), stress-free boundary conditions are prescribed on the upper surface Γ_s, and periodic boundary conditions are prescribed on the lateral boundaries Γ_l.

Figure 6 compares the solution computed within the *Albany/FELIX* code for ISMIP-HOM test A with the solution computed by the code of (Perego et al., 2012) (denoted by MP12 in this figure). The agreement between the two is excellent. The second column of Table 2 reports the relative difference between these two solutions in the l^2 norm (24). The relative difference is at most 0.1% for $L = 180$ and on the order of 0.001% for $L = 5, 10, 20, 40$.

Figure 6 also includes the mean and standard deviation of solutions computed by other models participating in the original set of benchmark experiments. For a detailed description of these models the reader is referred to (Pattyn et al., 2008). For all values of L considered, the *Albany/FELIX* solution is within one standard deviation of the mean of the other FO models considered in the original set of experiments. In Figure 6, the solutions labeled "Full Stokes" were calculated using

the (more expensive but more physically realistic) full Stokes model for ice sheet flow (detailed in Appendix A). Comparing a FO Stokes solution to the full Stokes solution reveals how well the FO Stokes physics approximate the full Stokes model. The reader can observe by examining Figure 6 that agreement between the FO Stokes and the full Stokes solutions improves with increasing L.

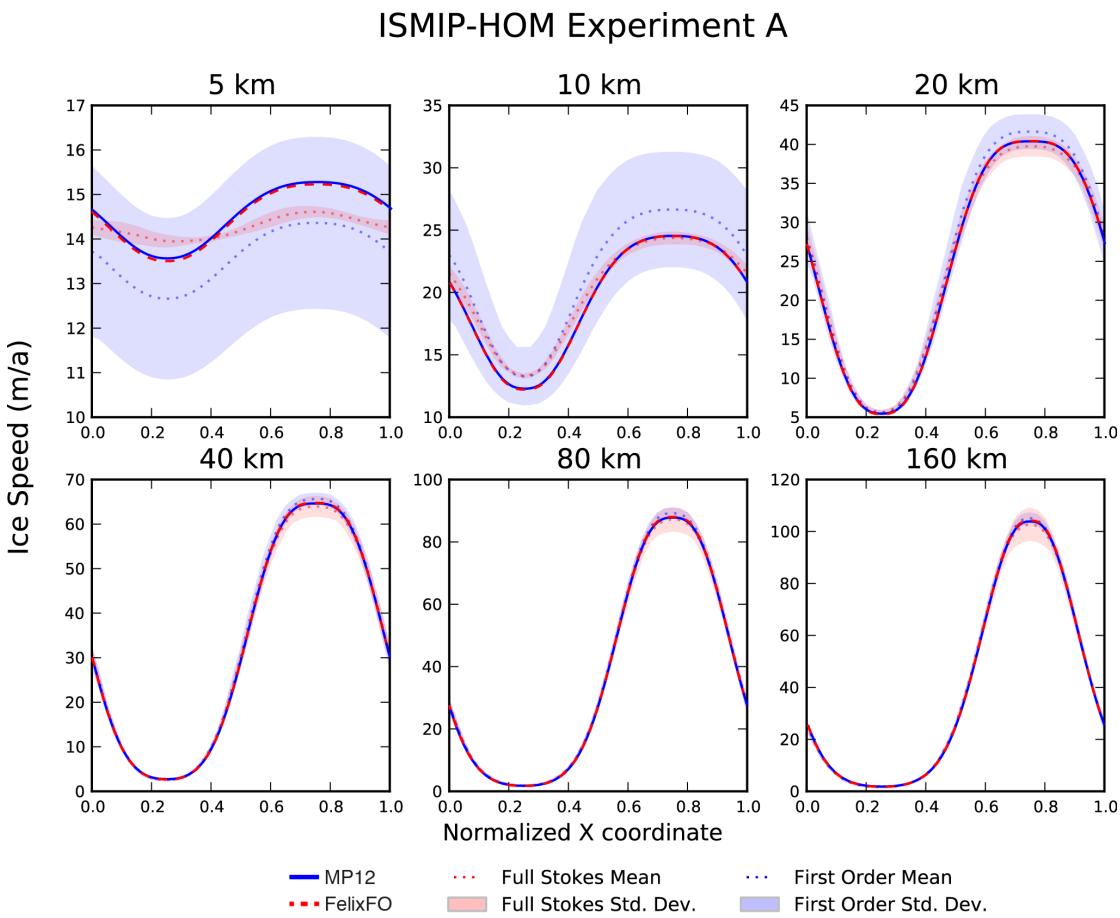

Fig. 6. ISMIP-HOM test A: surface velocity component u as a function of x at $y = L/4$ for each L considered. The blue solid line (MP12) represents results from (Perego et al., 2012) and the red-dashed line (labeled FelixFO) represents results from the current solver.

5.1.2 ISMIP-HOM test C

For ISMIP-HOM test C, the upper and bedrock surfaces (Γ_s and Γ_b, respectively) are given by the following linear functions:

$$s(x,y) = -x \tan\alpha, \qquad b(x,y) = s(x,y) - 1, \tag{39}$$

with $\alpha = 0.1°$. In addition to having a different geometry than test A, test C also differs in the boundary conditions. Unlike test A, sliding boundary conditions are prescribed on the bedrock ($\Gamma_\beta \equiv \Gamma_b$ and $\Gamma_0 \equiv \emptyset$), with the basal sliding coefficient given by

$$\beta(x,y) = 1 + \sin\left(\frac{2\pi}{L}x\right)\sin\left(\frac{2\pi}{L}y\right). \tag{40}$$

The boundary conditions at the upper and lateral boundaries (Γ_s and Γ_l respectively) are the same as for test A, namely stress-free and periodic, respectively. The geometry is thus that of a constant thickness, uniformly sloping slab along the x coordinate direction with a doubly periodic, "egg crate" spatial pattern for the basal friction parameter β.

The test case solution computed in *Albany/FELIX* is shown in Figure 7, along with the solution computed using the solver of (Perego et al., 2012). For every L considered, the relative difference between *Albany/FELIX* and the solver of (Perego et al., 2012) (denoted, as before, by MP12 in Figure 7) is less than 1% (Table 2). Moreover, as for ISMIP-HOM test A, the *Albany/FELIX* solution is within one standard deviation of the model means for each value of L. As for ISMIP-HOM test A, Figure 7 illustrates also how well the FO Stokes model compares to the (more expensive but more accurate) full Stokes model. As for test A, the two models agree better for larger L.

Table 2. Relative differences between *Albany/FELIX* and (Perego et al., 2012) solutions for ISMIP-HOM tests A and C

L (km)	Test A	Test C
5	0.00735%	0.386%
10	0.00629%	0.248%
20	0.00132%	0.176%
40	0.00408%	0.213%
80	0.0407%	0.277%
160	0.127%	0.320%

5.2 Confined shelf benchmark

We next consider an idealized ice shelf test case, referred to here as the "confined shelf" test case, which is a slightly modified version of test 3 from the Ice Shelf Model Intercomparison exercise (Rommelaere, 1996). The geometry is that of a 500 m thick slab of ice with equal extents of 200 km along the x– and y–dimensions, floating in hydrostatic equilibrium (Figure 8). A stress-free boundary condition is applied at the upper and basal boundaries ($z = s$ and $z = b$ respectively) and homogeneous Dirichlet boundary conditions ($u = v = 0$) are applied on three of the four lateral boundaries (the east $x = 200$, west $x = 0$ and north $y = 200$ boundaries). The south ($y = 0$) lateral

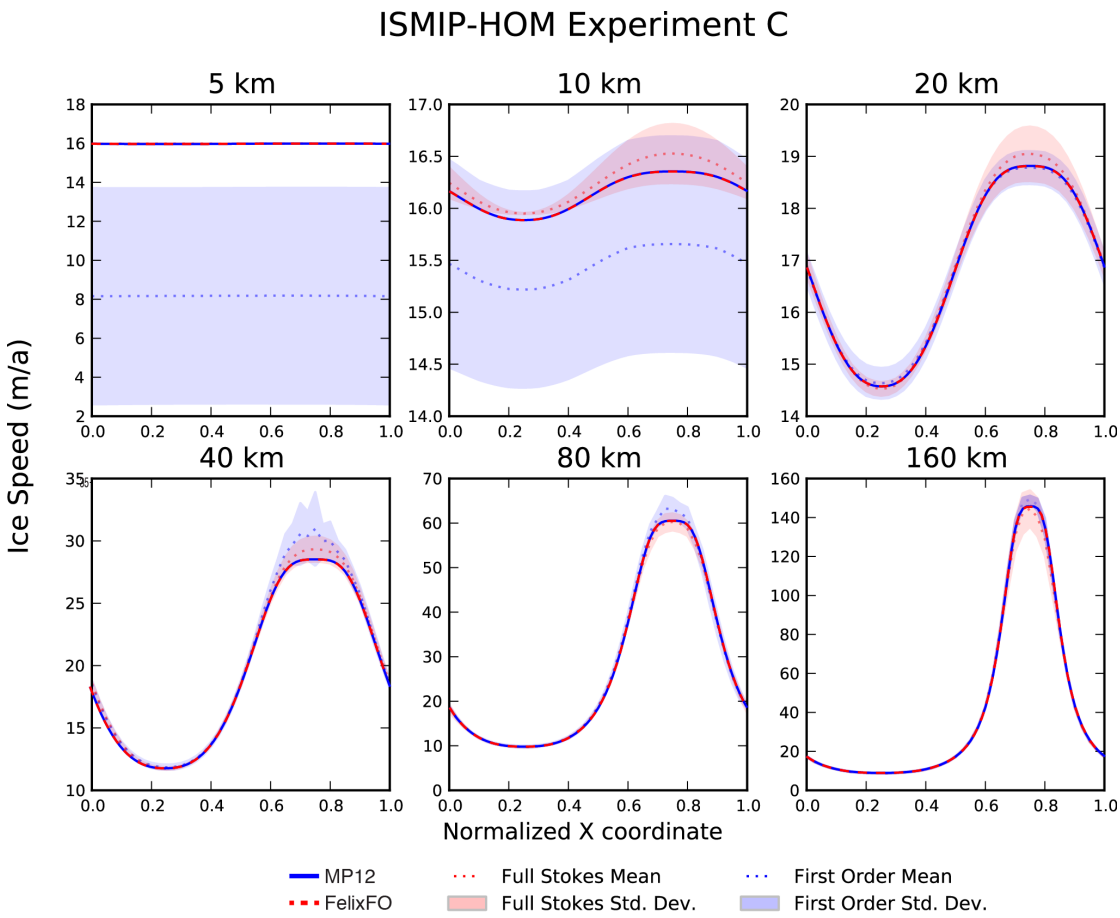

Fig. 7. ISMIP-HOM test C: surface velocity component u as a function of x at $y = L/4$ for each L considered. The blue solid line (MP12) represents results from (Perego et al., 2012) and the red-dashed line (labeled FelixFO) represents results from the current solver. Note that for the 5 km test, the MP12 and FelixFO results directly overly the results for the full Stokes models participating in the original intercomparison.

boundary is open to the ocean and subject to the open ocean Neumann boundary condition described in Section 2 (boundary condition (c)). The values of the parameters that appear in (17) can be found in Table 1. The domain and boundary faces for the confined shelf problem are illustrated in Figure 8.

The confined shelf geometry is discretized using a structured tetrahedral mesh of 41×41 nodes in the $x - y$ plane with 10 vertical levels. As with the ISMIP-HOM test cases, the solution for the confined shelf test case computed in our code, *Albany/FELIX*, is compared to the solution computed by the solver of (Perego et al., 2012) on the same mesh. Figure 9(a) shows the solution calculated in *Albany/FELIX*, which is visually identical to the solution computed by the solver of (Perego et

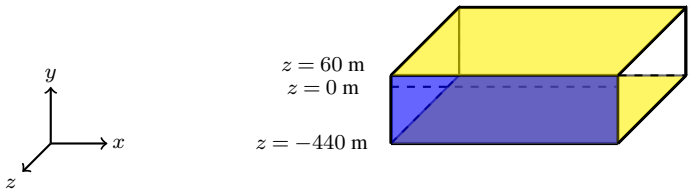

Fig. 8. Illustration of domain and boundaries for confined shelf problem: stress-free boundaries (yellow), Dirichlet lateral boundaries (white), open-ocean lateral boundary (blue) [*Note: Figure not drawn to scale.*]

al., 2012). Figure 9(b) shows the difference between the *Albany/FELIX* and (Perego et al., 2012) solutions, which are on the order of $\mathcal{O}(10^{-10})$.

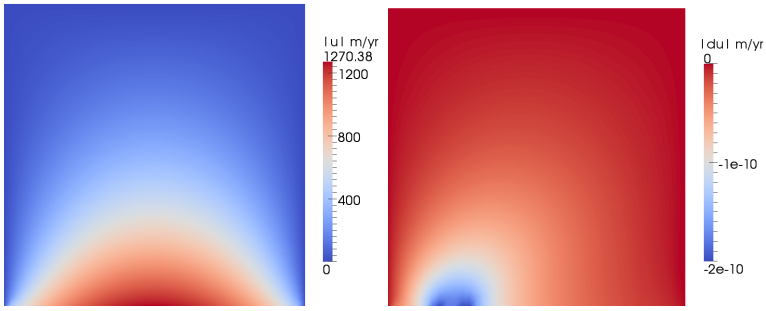

(a) (b)

Fig. 9. Solution to confined-shelf test case: (a) *Albany/FELIX*, (b) Difference between *Albany/FELIX* and the solver of (Perego et al., 2012).

6 Convergence study using realistic geometry

The final results presented herein are the results of a numerical convergence and performance study using a realistic, 1 km spatial resolution Greenland Ice Sheet (GIS) geometry (i.e., surface and bed topography from (Bamber et al., 2013)).

6.1 Full 3D convergence study

First, we present results from a 3D mesh convergence study in which a set of horizontal uniform quadrilateral meshes of different resolutions were considered. We began by generating a quadrilateral mesh having an 8 km horizonal resolution. We then refined this coarse mesh uniformly in the horizontal direction (by splitting each quadrilateral finite element into four smaller quadrilaterals) four times to yield meshes with resolutions of 4 km, 2 km, 1 km and 500 m. The horizontal meshes were then extruded into 3D hexahedral meshes having uniform layers. The number of layers considered in this study ranges from 5 to 80. Realistic basal friction coefficient (β) fields and bed topographies were calculated by solving a deterministic inversion problem that minimizes simultaneously the discrepancy between modeled and observed surface velocities, modeled and observed bed topography, and between a specified surface mass balance field and the modeled flux divergence (see (Perego et al., 2014) for more details). A realistic, 3D temperature field, originally calculated using the Community Ice Sheet Model (CISM) for the study in (Shannon et al., 2013), was included as an initial condition in order to provide realistic values for the flow-law rate factor (9). Prior to being interpolated onto the meshes at hand, the original topography, surface height, basal friction and temperature data were smoothed by convolution with a 2D Gaussian filter (having a standard deviation of 5 km). This smoothing filter reduces the small-scale variations of the original fields, so that it is reasonable to consider meshes from 8 km to 500 m for our convergence study. Using directly the non-smoothed data, we would have needed to consider much finer meshes in order to obtain asymptotic convergence. Table 3 summarizes the meshes considered and the related degrees of freedom (dofs)

Table 3. Meshes used in the GIS full, 3D convergence study.

horizontal resolution	# vertical layers	# dofs	# cores	$\mathcal{E}_{rel}^{cont}$
8 km	5	3.34K	4	3.22×10^{-1}
4 km	10	2.43M	32	1.28×10^{-1}
2 km	20	18.4M	256	3.70×10^{-2}
1 km	40	143M	2048	8.49×10^{-3}
500 m	80	1.12B	16,384	–

For the convergence study undertaken here, the objective is to show a theoretical convergence rate for the finite elements evaluated. From finite element theory, theoretical convergence rates are expected for a problem in which the data is fixed on all meshes considered, so better-resolved data are intentionally not introduced on the coarser meshes that were part of our convergence study in this section. A high-resolution GIS problem, with real, high-resolution data is considered in Section 6.3.3.

The FO equations (2) with basal sliding at the bedrock (15) and stress-free boundary conditions (14) on the remaining boundaries were solved on the base 8 km resolution mesh and the four successively refined meshes. Model runs were performed in parallel on *Titan*[2], a Cray XK6 operated by the Oak Ridge Leadership Computing Facility (OLCF). The fourth column of Table 3 reports the number of CPU cores used for each mesh resolution. Note that the parallel decompositions employed in the runs were 2D only; all elements with the same x and y coordinates were on the same processor (convergence difficulties were encountered when splitting vertical columns in the mesh across processors). A parallel decomposition for 16 cores is illustrated in Figure 11.

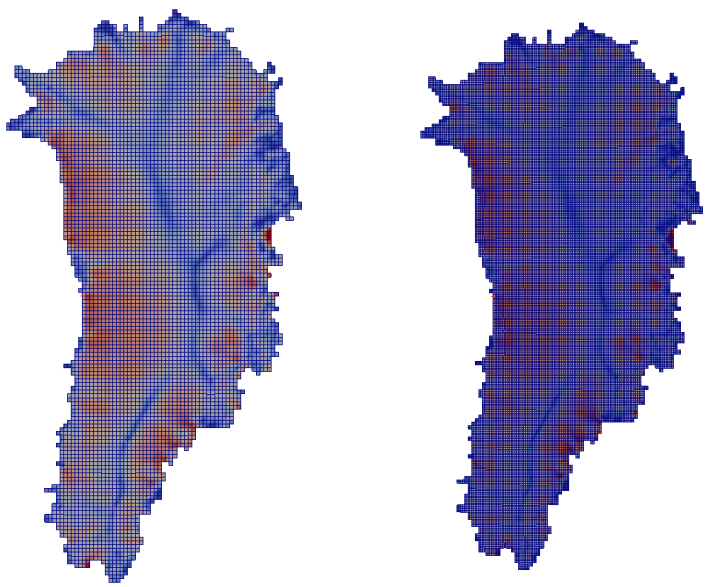

(a) (b)

Fig. 10. Examples of uniform mesh refinement: (a) No refinement (8 km GIS), (b) 1 level of refinement (4 km GIS)

The last column of Table 3 reports the relative errors in the computed solution for each mesh resolution considered. The convergence metric employed was the continuous L^2 norm. The relative error in each solution was calculated according to the following formula:

$$\mathcal{E}_{rel}^{cont} \equiv \sqrt{\frac{\int_\Omega ||\mathbf{u}_n - \mathbf{u}_{ref}||_2^2 d\Omega}{\int_\Omega ||\mathbf{u}_{ref}||_2^2 d\Omega}}. \tag{41}$$

In (41), $||\cdot||_2$ denotes the L^2 norm, $\mathbf{u}_n$ denotes the computed solution and $\mathbf{u}_{ref}$ denotes the reference solution, which here we take as the solution computed for the finest resolution mesh (for this quasi-

[2]More information on *Titan* can be found at www.olcf.ornl.gov/titan.

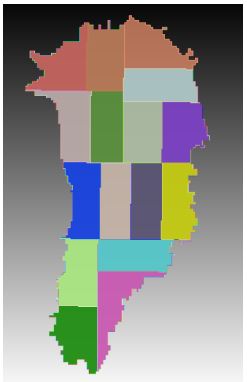

Fig. 11. GIS domain decomposition for 16 core, parallel run, with different colors representing portions of the domain owned by different cores.

realistic problem, there is no exact solution available in closed analytic form). The integrals in (41) were calculated exactly using a sufficiently accurate numerical quadrature rule.

Figure 12 plots the relative error (41) as a function of the horizontal mesh spacing (8 km, 4 km, 2 km, 1 km) on a log-log plot (blue line). The numerical values of the relative error $\mathcal{E}_{rel}$ are reported in the right-most column of Table 3. The asymptotic convergence rate (the slope of the blue line in Figure 12 disregarding the coarsest mesh data point, as it is not in the region of asymptotic convergence) is 1.96. This compares very well with the theoretical convergence rate of two, for the bilinear hexahedral elements considered in this norm (black-dashed line in Figure 12).

6.2 Convergence study with z–refinement

Next, we perform a convergence study with respect to the number of vertical layers, that is, a convergence study with refinement in the z direction only. To the authors' knowledge, the answer to the question of how many vertical layers should be used in large-scale ice sheet simulations (e.g., of Greenland or Antarctica) remains open. Many researchers employ a fixed number (usually on the order of 10, e.g., (Lemieux, 2011)) regardless of the horizontal resolution of the mesh. Sometimes this choice is motivated by solver convergence difficulties encountered when a larger number of vertical layers are used (e.g., (Larour et al., 2012b)). The purpose of our mesh convergence study with respect to the number of vertical layers is two-fold:

(i) To determine in a rigorous fashion for a GIS problem with a fixed horizontal mesh resolution how many vertical layers are required to achieve a solution having a desired accuracy,

(ii) To investigate whether the performance of our linear and nonlinear solvers changes with the number of vertical layers.

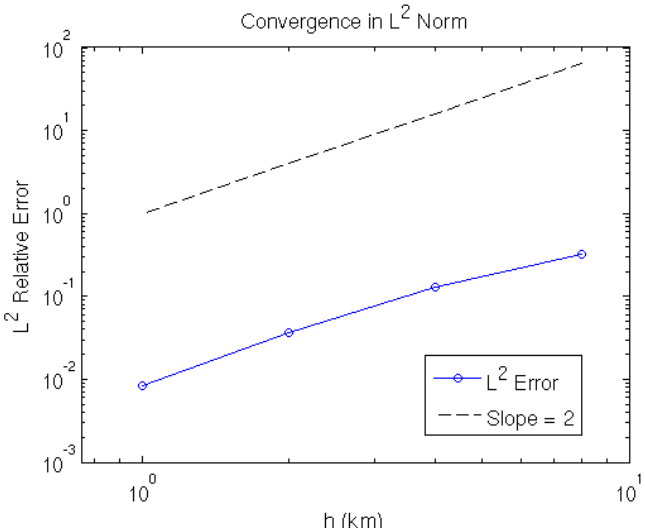

Fig. 12. Convergence in the continuous L^2 norm (41) for the realistic GIS problem with full 3D refinement.

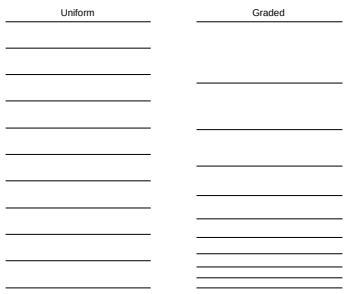

Fig. 13. Uniform (left) versus graded (right) spacing in the vertical layers.

For our convergence study with respect to z–refinement, we consider the full, 1 km resolution (in the $x-y$ plane) data from (Bamber et al., 2013) along with realistic, 2D basal friction coefficient (β)

and 3D internal temperature fields, as discussed above. Two vertical mesh spacings are considered:

(a) Uniform spacing in z.

(b) Graded spacing in z.

In the latter case, a transformation is performed such that a mesh having n_z vertical layers is finer near the bedrock boundary Γ_b and becomes progressively coarser moving up, towards the surface boundary Γ_s. The formulas for the coordinate of the ith vertical layer, z_i (for $i = 0, ..., n_z$, where n_z is the number of vertical layers), for each of these two spacings is given in Table 4. Figures 13(a) and (b) show the uniform vs. graded z–spacing, respectively[3]. Twelve instances of the 1 km GIS

Table 4. Formulas for different vertical mesh-spacing strategies (uniform vs. graded), for $i = 0, ..., n_z$.

z–spacing	z_i
Uniform	$\frac{i}{n_z}$
Graded	$1 - \frac{4}{3}\left[1 - \left(\frac{n_z}{2n_z - i}\right)^2\right]$

problem are considered, each with a different number of vertical layers (resolution in z): 5, 10, 20, 40, 80 and 160 vertical layers, with both uniform and graded spacing in z (Table 5).

Table 5. Meshes considered for 1 km resolution, z–refinement (refinement in # vertical layers) convergence study.

# vertical layers	# dofs	# cores	$\mathcal{E}_{rel}^{cont}$: uniform spacing	$\mathcal{E}_{rel}^{cont}$: graded spacing
5	21.0M	128	3.17×10^{-2}	2.54×10^{-2}
10	38.5M	256	8.04×10^{-3}	6.56×10^{-3}
20	73.5M	512	2.01×10^{-3}	1.64×10^{-3}
40	143M	1024	4.96×10^{-4}	3.93×10^{-4}
80	283M	2048	1.20×10^{-4}	8.03×10^{-5}
160	563M	16,384	2.76×10^{-5}	–

As for the full 3D convergence study, 2D decompositions of the domain were generated (Figure 11). For the error analysis as a function of mesh spacing, we take the 160 vertical layer mesh with graded spacing as the reference solution in (41). The last two columns of Table 5 report the relative errors as a function of the z–resolution for the uniform and graded mesh spacings. These errors are plotted in Figure 14 as a function of the z–resolution $\Big($denoted by h_z, taken to be the reciprocal

[3]The formula for the graded z–spacing is available in the CISM documentation, available at http://oceans11.lanl.gov/cism.

of the number of vertical layers, i.e., $h_z = \frac{1}{5}, \frac{1}{10}, \frac{1}{20}, \ldots\Big)$. Convergence rates can be obtained by calculating the slopes of the red and blue lines in Figure 14. Omitting the data points for the finest mesh resolution[4], the observed convergence rates are calculated to be 2.0096 for the uniform mesh spacing (slope of blue line in Figure 14) and 2.0041 for the graded mesh spacing (slope of red line in Figure 14), in excellent agreement with the expected convergence rate of 2.

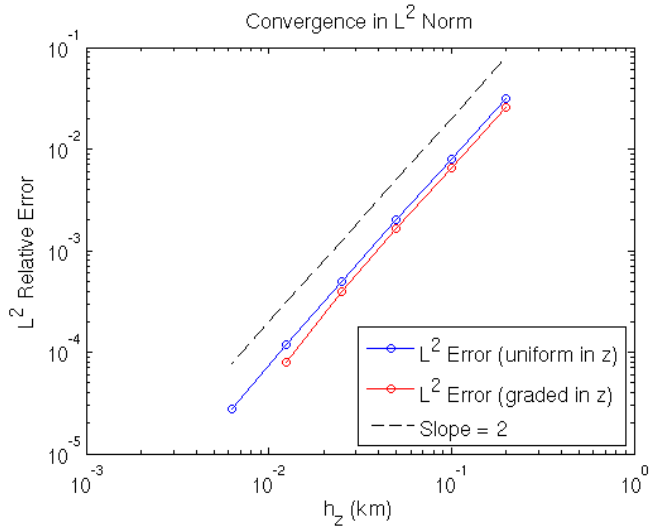

Fig. 14. Convergence in continuous L^2 norm (41): z–refinement (number of vertical layers)

The results summarized above led to some practical recommendations that may be of interest to the glaciological modeling community. First, if a relative error of less than $\mathcal{O}(10^{-3})$ is desired for a GIS problem discretized by a mesh of linear (or trilinear) finite elements[5] with a 1 km spatial mesh resolution, more than 10 vertical layers should be used in the full 3D mesh for this geometry. Moreover, as noted in the discussion of the full 3D mesh convergence study described in Section 6.1, our study revealed that 2D parallel decompositions of the meshes (i.e., decompositions in which all elements with the same x and y coordinates were on the same processor, as shown in Figure 11) led to out-of-the-box convergence of our linear and nonlinear solves. In contrast, convergence difficulties were encountered when splitting vertical columns in the mesh across processors. The 2D parallel decomposition is therefore recommended over a full 3D parallel decomposition, especially for problems on meshes having a finer vertical resolution.

[4]Including this data point will result in an over-estimation of the convergence rate since a reference solution is used in place of the exact solution in the error calculation.

[5]Note that if higher-order elements are considered, as in the work of (Leng et al., 2014; Isaac et al., 2014), the recommended number of layers would likely be smaller.

6.3 Code performance and scalability

Having demonstrated the numerical convergence of our code on a realistic, large-scale ice sheet problem we now study the code's robustness, performance and scalability.

6.3.1 Robustness

In Section 3.1.1, we described our approach for improving the robustness of the nonlinear solver using a homotopy continuation of the regularization parameter (denoted by γ) appearing in the effective viscosity law expression (21). Here, we perform a numerical study of the relative robustness of Newton's method with and without the use of this continuation procedure on a realistic, 5 km resolution Greenland ice sheet problem. Three approaches are considered:

(a) Full Newton with no homotopy continuation.

(b) Newton with backtracking but no homotopy continuation.

(c) Full Newton with homotopy continuation.

For all three methods, a uniform velocity field is specified as the initial guess for Newton's method. To prevent the effective viscosity (7) from evaluating to "not-a-number" for this initial guess, we replace μ by μ_γ in (2), where μ_γ is given by (21) and $\gamma = 10^{-10}$ for the first two approaches. The third approach implements Algorithm 1, in which we use a natural continuation algorithm to reach $\gamma = 10^{-10}$ starting withza $\alpha_0 = 0.1$.

Figure 15 illustrates the performance of Newton's method for the three approaches considered by plotting the norm of the residual as a function of the total number of Newton iterations. The reader can observe that full Newton with no homotopy continuation diverges. If backtracking is employed, the algorithm converges to a tolerance of 10^{-4} in 43 nonlinear iterations. With the use of homotopy continuation, the number of nonlinear iterations is cut almost in half, to 24 nonlinear iterations. The natural continuation method leads to four homotopy steps.

It is well-known that for Newton's method to converge to the root of a nonlinear function (i.e., the solution to the discrete counterpart of (20)), it must start with an initial guess which is reasonably close to the sought-after solution. The proposed homotopy continuation method is particularly useful in the case when no "good" initial guess is available for Newton's method, in which case the nonlinear solver may fail to converge (see Section 3.1.1 and Algorithm 1). Homotopy continuation may not be needed for robust convergence in the case that a "good" initial guess *is* available (e.g., from observations or from a previously converged model time step).

6.3.2 Controlled weak scalability study on successively refined meshes with coarse mesh data

First, we report results for a controlled weak scalability study. For this experiment, the 8 km GIS mesh with 5 vertical layers described in Section 6.1 was scaled up to a 500 m GIS mesh with 80

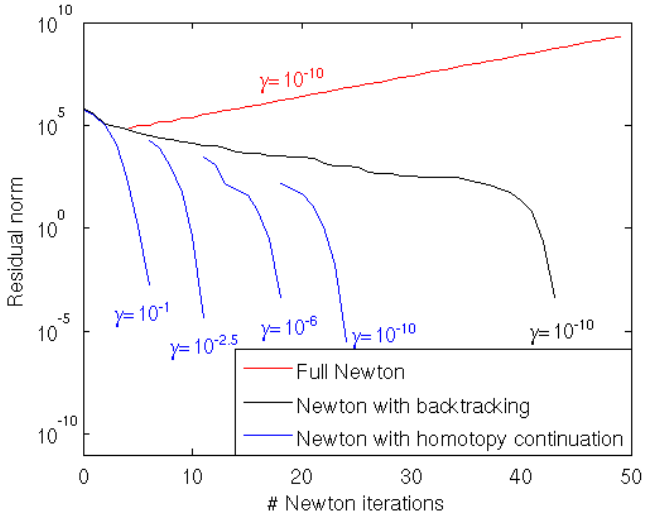

Fig. 15. Robustness of Newton's method nonlinear solves with homotopy continuation

vertical layers using the uniform 3D mesh refinement discussed earlier. A total of five meshes were generated, as summarized in Table 3. The term "controlled" refers to the fact that the lateral boundary of the ice-sheet is kept constant for all the grids considered and equal to the polygonal boundary determined by the coarsest 8km mesh. Moreover, topography, surface height, basal friction and temperature data have been smoothed and then interpolated as described in Section 6.1. Each resolution problem was run in parallel on the *Hopper*[6] Cray XE6 supercomputer at the National Energy Research Scientific Computing (NERSC) Center. The number of cores for each run (third column of Table 3) was calculated so that for each size problem, each core had approximately the same number of dofs ($\approx 70-80$K dofs/core). For a detailed discussion of the numerical methods employed, the reader is referred to Section 3. In particular, recall that the linear solver employed is based on the preconditioned CG iterative method. The preconditioner employed is the algebraic multilevel preconditioner based on the idea of semi-coarsening that was described in Section 3.1.2. This preconditioner is available through the *ML* package of *Trilinos* (Heroux et al., 2005).

Figure 16(a) reports the total linear solver time, the finite element (FE) assembly time and the total time (in seconds) for each resolution problem considered, as a function of the number of cores. Figure 16(b) shows more detailed timing information, namely:

- The normalized preconditioner generation time ("Prec Gen Time").

[6]More information on the *Hopper* machine can be found here: http://www.nersc.gov/users/computational-systems/hopper.

- The normalized Jacobian fill time, not including the Jacobian export time[7] ("Jac Fill - Jac Export Time").
- The normalized number of nonlinear solves ("# Nonlin Solves").
- The normalized average number of linear iterations ("Avg # Lin Iter").
- The normalized total time not including I/O ("Total Time - IO").

The run times and iteration counts have been normalized by the run time and iteration count (respectively) for the smallest run (8 km GIS with 5 vertical layers, run on 4 cores). Figure 16 reveals that the run times and iteration times scale well, albeit not perfectly, in a weak sense.

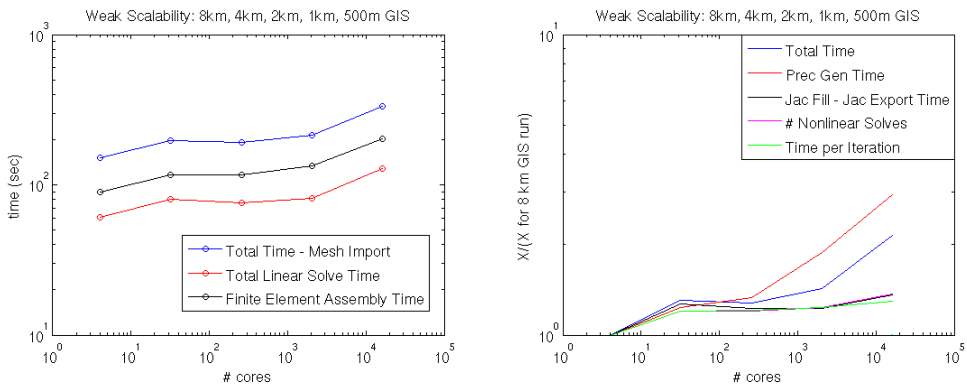

(a) (b)

Fig. 16. Controlled, weak scalability study on *Hopper*: (a) Total linear solve, finite element assembly, and total run times in seconds , (b) Additional timing information (X = time or # iterations).

6.3.3 Strong scalability for realistic Greenland initial conditions on a variable-resolution mesh

For the performance study described in the previous paragraph, the data has been smoothed and the lateral boundary was determined by the coarsest (8 km resolution) mesh. We now perform a scalability study for the GIS interpolating directly original datasets into the mesh considered. This results in better resolved topography, basal friction and temperature fields. As before, the surface topography and temperature fields are from (Bamber et al., 2013) and were generated as a part of the

[7]"Jacobian export time" refers to the time required to transfer ("export") data from an element-based decomposition, which can be formed with no communication, to a node-based decomposition, where rows of the matrix are uniquely owned by a single processor.

Ice2Sea project (Ice2sea, 2014); the basal friction coefficient (β) field and the bed topography were calculated in (Perego et al., 2014).

We consider a tetrahedral mesh with a variable resolution of between 1 km and 7 km and having approximately 14.4 million elements, leading to approximately 5.5 million dofs (Figure 17(a)). The mesh was created by first meshing the base of the GIS using the 2D meshing software *Triangle* (Shewchuk et al., 1996). The 2D mesh generated using *Triangle* was a nonuniform Delaunay triangulation in which the areas of the triangles were constrained to be roughly proportional to the norm of the gradient of the surface velocity data. This yields meshes with better resolutions in places where the solution has larger variations. The 2D mesh is then extruded in the z–direction as prisms and each prism is divided into three tetrahedra (Figure 17(b)).

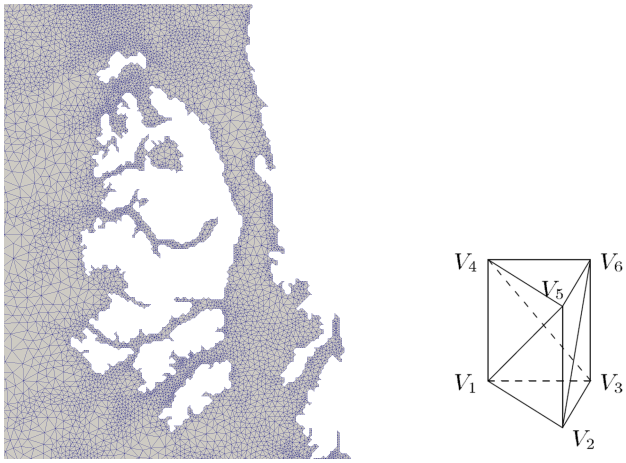

(a) (b)

Fig. 17. (a) Close-up of variable-resolution 1–7 km GIS mesh, (b) Subdivision of hexahedral finite element into three tetrahedra.

First, we verify that the solution computed on the 1–7 km variable resolution tetrahedral mesh – the modeled surface velocity field – agrees well with that from observations (Joughin et al., 2010). The solution computed on this mesh is shown in Figure 18(a). The reader can observe that this solution is in excellent agreement with the target velocity field from observations, shown in Figure 18(b).

Next, a strong scaling study on the 1–7 km variable resolution GIS problem is performed. The problem is run on different numbers of cores on *Hopper*, from 64 to 512. The total solve, linear solve and finite element assembly times for each of the runs are reported (in seconds) in Table 6. The speed-up relative to the smallest (64 core) run is plotted as a function of the number of cores in Figure 19. Good strong scalability is obtained: a 3.75 times speed-up is observed with 4 times the

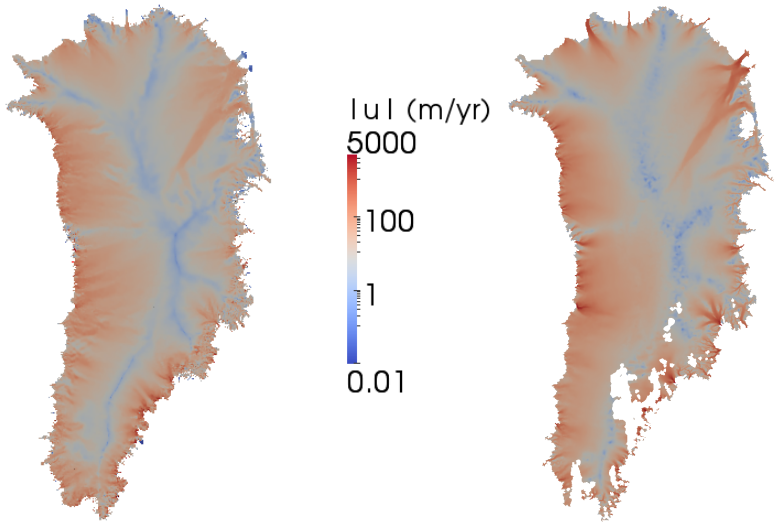

(a) (b)

Fig. 18. Solution magnitude $|\mathbf{u}|$ in meters per year: (a) *Albany/FELIX* solution (surface speed) on the variable resolution (1–7 km) tetrahedral mesh, (b) observed surface speeds (from (Joughin et al., 2010)).

number of cores (up to and including 256 cores), and a 6.64 times speed-up is observed with 8 times the number of cores (up to and including 512 cores). In these results, the linear solver employed was the preconditioned CG iterative method, with the aforementioned algebraic multilevel preconditioner based on the idea of semi-coarsening (see Section 3.1.2).

Table 6. Total, linear solve and finite element assembly times (sec) for variable resolution 1–7 km resolution GIS problems as a function of # cores of *Hopper*

# cores	Total Solve Time	Linear Solve Time	Finite Element Assembly Time
64	268.1	119.9	148.3
128	139.9	63.12	76.78
256	78.41	37.92	40.49
512	56.83	33.81	23.02

7 Conclusions

In this paper, we have presented a new, parallel, finite element solver for the first-order accurate, nonlinear Stokes ice sheet model. This solver, *Albany/FELIX*, has been written using a component-

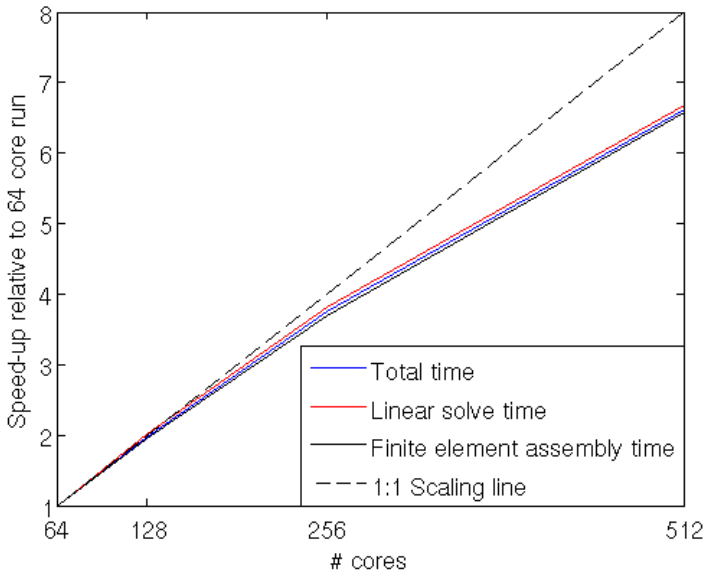

Fig. 19. Strong scalability for 1–7km resolution GIS problem: speed-up relative to 64 core run.

based approach to building application codes. The components comprising the code are modular *Trilinos* libraries, which are put together using abstract interfaces and Template-Based Generic Programming. Several verifications of the code's accuracy and convergence are carried out. First, a mesh convergence study is performed on several new method of manufactured solutions test cases derived for the first-order Stokes equations. All finite elements tested exhibit their theoretical rate of convergence. Next, code-to-code comparisons are made on several canonical ice sheet benchmarks between the *Albany/FELIX* code and the finite element solver of (Perego et al., 2012). The solutions are shown to agree to within machine precision. As a final verification, a mesh convergence study on a realistic Greenland geometry is performed. The purpose of this test is two-fold: (1) to demonstrate that the solution converges at the theoretical rate with mesh refinement, and (2) to determine how many vertical layers are required to accurately resolve the solution with a fixed x–y resolution, when using (low-order) trilinear finite elements. It is found that the parallel decomposition of a mesh has some effect on the linear and nonlinear solver convergence: better performance is observed on the finer meshes if a horizontal decomposition (i.e., a decomposition in which all nodes having the same x and y coordinates are on the same processor) is employed for parallel runs. Further performance studies reveal that a robust nonlinear solver is obtained through the use of homotopy continuation with respect to a regularization parameter in the effective viscosity in the governing equations, and that good weak scalability can be achieved by preconditioning the iterative linear solver using an

algebraic multilevel preconditioner constructed based on the idea of semi-coarsening.

Appendix A: Nonlinear Stokes model for glaciers and ice sheets

The model considered here, referred to as the first-order (FO) Stokes approximation, or the "Blatter-Pattyn" model (Blatter, 1995; Pattyn, 2003), is an approximation of the nonlinear Stokes model for glacier and ice sheet flow. In general, glaciers and ice sheets are modeled as an incompressible fluid in a low Reynolds number flow with a power-law viscous rheology, as described by the Stokes flow equations. The equations are quasi-static, as the inertial and advective terms can be neglected due to the slow movement of the ice.

Let $\boldsymbol{\sigma}$ denote the Cauchy stress tensor, given by

$$\boldsymbol{\sigma} = 2\mu\dot{\boldsymbol{\epsilon}} - p\mathbf{I} \in \mathbb{R}^{3\times 3}, \tag{42}$$

where μ denotes the "effective" ice viscosity, p the ice pressure, $\mathbf{I}$ the identity tensor, and $\dot{\boldsymbol{\epsilon}}$ the strain-rate tensor:

$$\dot{\epsilon}_{ij} = \frac{1}{2}\left(\frac{\partial u_i}{\partial x_j} + \frac{\partial u_j}{\partial x_i}\right), \tag{43}$$

for $i, j \in \{1, 2, 3\}$. The effective viscosity is given by Glen's law (Nye, 1957; Cuffey et al., 2010):

$$\mu = \frac{1}{2}A^{-\frac{1}{n}}\dot{\epsilon}_e^{\left(\frac{1}{n}-1\right)}, \tag{44}$$

where

$$\dot{\epsilon}_e = \sqrt{\frac{1}{2}\sum_{ij}\dot{\epsilon}_{ij}^2}, \tag{45}$$

denotes the effective strain rate, given by the second invariant of the strain-rate tensor. A denotes the flow rate factor (which is strongly dependent on the ice temperature), and n denotes the power law exponent (generally taken equal to 3). The nonlinear Stokes equations for glacier and ice sheet flow can then be written as follows:

$$\begin{cases} -\nabla\cdot\boldsymbol{\sigma} = \rho\mathbf{g} \\ \nabla\cdot\mathbf{u} = 0. \end{cases} \tag{46}$$

Here, ρ denotes the ice density, and $\mathbf{g}$ the gravitational acceleration vector, i.e., $\mathbf{g}^T = \Big(0,\, 0,\, -g\Big)$, with g denoting the gravitational acceleration. The values of the parameters that appear in the expressions above are given in Table 1. A stress-free boundary condition is prescribed on the upper surface:

$$\boldsymbol{\sigma}\mathbf{n} = \mathbf{0}, \text{ on } \Gamma_s. \tag{47}$$

On the lower surface, the relevant boundary condition is the no-slip or basal sliding boundary condition:

$$\begin{cases} \mathbf{u} = \mathbf{0}, & \text{on } \Gamma_0, \\ \mathbf{u} \cdot \mathbf{n} = 0 \text{ and } (\boldsymbol{\sigma}\mathbf{n} + \beta\mathbf{u})_{||} = \mathbf{0}, & \text{on } \Gamma_\beta, \end{cases} \tag{48}$$

assuming $\Gamma_b = \Gamma_0 \cup \Gamma_\beta$ with $\Gamma_0 \cap \Gamma_\beta = \emptyset$, where $\beta \equiv \beta(x, y) \geq 0$. The operator $(\cdot)_{||}$ in (48) performs the tangential projection onto a given surface.

Acknowledgements

Support for all authors was provided through the Scientific Discovery through Advanced Computing (SciDAC) program funded by the U.S. Department of Energy (DOE), Office of Science, Advanced Scientific Computing Research and Biological and Environmental Research. This research used resources of the National Energy Research Scientific Computing Center (NERSC; supported by the Office of Science of the U.S. Department of Energy under Contract DE-AC02-05CH11231) and the Oak Ridge Leadership Computing Facility (OLCF; supported by the DOE Office of Science under Contracts DE-AC02-05CH11231 and DE-AC05-00OR22725). The authors thank M. Norman of Oak Ridge National Laboratory for generation of the Greenland geometry datasets, J. Johnson (and students) of the University of Montana for initial development of the ISMIP-HOM plotting scripts, and M. Hoffman and B. Lipscomb at Los Alamos National Laboratory for useful discussions that led to some of the ideas and results presented in this paper.

References

B. Adams, L. Bauman, W. Bohnhoff, K. Dalbey, M. Ebeida, J. Eddy, M. Eldred, P. Hough, K. Hu, J. Jakeman, L. Swiler, and D. Vigil, DAKOTA, A Multilevel Parallel Object-Oriented Framework for Design Optimization, Parameter Estimation, Uncertainty Quantification, and Sensitivity Analysis: Version 5.4 User's Manual, *Sandia Technical Report SAND2010-2183*, December 2009. Updated April 2013.

E. Allgower, and K. Georg, Introduction to Numerical Continuation Methods, *SIAM Classics in Applied Mathematics*, **45** (2003).

S. Balay, K. Buschelman, V. Eijkhout, W. Gropp, D. Kaushik, M. Knepley, L. McInnes, B. Smith, H. Zhang, PETSc Users Manual, *Technical Report ANL-95/11, Revision 3.0.0*, Argonne National Laboratory, Lemont, IL (2008).

J. Bamber, J Griggs, R. Hurkmans, J. Dowdeswell, S. Gogineni, I. Howat, J. Mouginot, J. Paden, S. Palmer, E. Rignot, and D. Steinhage, A new bed elevation dataset for Greenland, *Cryosphere*, **7**(2), 499–510 (2013).

E. Bavier. M. Hoemmen, S. Rajamanickam, and H. Thormquist, Amesos2 and Belos: Direct and iterative solvers for large sparse linear systems, *Sci. Program.*, **20**, 241–255 (2012).

H. Blatter, Velocity and stress fields in grounded glaciers: a simple algorithm for including deviatoric stress gradients, *J. Glaciol.*, **41**(138), 333–344 (1995).

P. Bochev, C. Edwards, R. Kirby, K. Peterson, and D. Ridzal, Solving PDEs with Intrepid, *Sci. Program.*, **20**, 151–180 (2012).

D. Brinkerhoff, and J. Johnson, Data assimilation and prognostic whole ice sheet modelling with the variationally derived, higher order, open source, and fully parallel ice sheet model VarGlaS, *Cryosphere*, **7** 1161–1184 (2013) doi:10.5194/tc-7-1161-2013.

British Antarctic Survey, ice2sea FP7 EU Project Homepage, March 2014, URL: http://www.ice2sea.eu.

P. Brown, R. Falgout, and J. Jones, Semicoarsening Multigrid on Distributed Memory Machines *SIAM J. Sci. Comput.*, **21**(5), 1823–1834 (2000).

J. Brown, B. Smith, and A. Ahmadia, Achieving textbook multigrid efficiency for hydrostatic ice sheet flow, *SIAM J. Sci. Comput.*, **35**(2), B359–B375 (2013).

E. Bueler, J. Brown, and C. Lingle, Exact solutions to the thermomechanically coupled shallow-ice approximation: effective tools for verification, *J. Glaciol.*, **53**, 499–516 (2007).

E. Bueler, and J. Brown, Shallow shelf approximation as a 'sliding law' in a thermomechanically coupled ice sheet model, *J. Geophys. Res.*, **114**, 1–21 (2009), doi:10.1029/2008JF001179.

Q. Chen, M. Gunzburger, and M. Perego, Well-Posedness Results for a Nonlinear Stokes Problem Arising in Glaciology, *SIAM J. Math. Anal.*, **45**(5), 2710–2733 (2013).

S. Cornford, D. Martin, D. Graves, D. Ranken, A. Le Brocq, R. Gladstone, A. Payne, J. Antony, E. Ng, and W. Lipscomb, Adaptive mesh, finite volume modeling of marine ice sheets, *J. Comput. Phys.*, **232**, 529–549 (2013), doi:10.1016/j.jcp.2012.08.037.

K. Cuffey, and W. Paterson, *The physics of glaciers*, 4th edition (Butterworth-Heinemann, Oxford, 2010).

J. Dendy and J. Moulton, Black box multigrid with coarsening by a factor of three, *Numer. Lin. Algebra Appl.*, **17**(2-3), 577–598 (2010).

J. Dukowicz, S. Price, and W. Lipscomb, Consistent approximations and boundary conditions for ice-sheet dynamics from a principle of least action, *J. Glaciol.*, **56**(197), 480–496 (2010).

J. Dukowicz, S. Price, and W. Lipscomb, Incorporating arbitrary basal topography in the variational formulation of ice-sheet models, *J. Glaciol.*, **57**(203), 461–467 (2011).

O. Gagliardini, T. Zwinger, F. Gillet-Chaulet, G. Durand, L. Favier, B. de Fleurian, R. Greve, M. Mallnen, C. Martin, P. Raback, J. Ruokolainen, M. Sacchettini, M. Schafer, H. Seddik, and J. Thies, Capabilities and performance of Elmer-Ice, a new-generation ice sheet model, *Geosci. Model Dev.*, **6**, 1299–1318 (2013), doi:10.5194/gmd-6-1299-2013.

X. Gao, E. Nielsen, R. Muller, R. Young, A. Salinger, N. Bishop, M. Lilly, and M. Carroll, Quantum computer aided design simulation and optimization of semiconductor quantum dots, *J. Appl. Phys.,* **114**(164302) 1–19 (2013).

F. Gillet-Chaulet, O. Gagliardini, H. Seddik, M. Nodet, G. Durand, C. Ritz, T. Zwinger, R. Greve, and D.G. Vaughan, Greenland ice sheet contribution to sea-level rise from a new-generation ice-sheet model, *Cryosphere*, **6**, 1561–1576 (2012), doi:10.5194/tc-6-1561-2012.

D. Goldberg, and O.Sergienko, Data assimilation using a hybrid ice flow model, *Cryosphere*, **5**, 315–327 (2011), doi:10.5194/tc-5-315-2011.

D. Goldberg, and P. Heimbach, Parameter and state estimation with a time-dependent ajdoint marine ice sheet model, *Cryosphere*, **6**, 1659–1678 (2013).

M. Hagdorn, I. Rutt, T. Payne, and F. Hebeler, Glimmer 1.5.1 Documentation, April 2010, URL: http://www.cesm.ucar.edu/models/cesm1.0/cism/docs/glimmer.pdf.

M. Heroux, R. Bartlett, V. Howle, R. Hoekstra, J. Hu, T. Kolda, R. Lehoucq, K. Long, R. Pawlowski, E. Phipps, A. Salinger, H. Thornquist, R. Tuminaro, J. Willenbring, A. Williams, and K. Stanley, An Overview of the Trilinos Project, *ACM Trans. Math. Softw.*, **31**(3), 397–423 (2005).

T. Hughes, The Finite Element Method: Linear Static and Dynamic Finite Element Analysis (Dover edition, 2000).

J. Hurrell, M. Holland, P. Gent, S. Ghan, J. Kay, P. Kushner, J.-F. Lamarque, W. Large, D. Lawrence, K. Lindsay, W. Lipscomb, M. Long, N. Mahowald, D. Marsh, R. Neale, P. Rasch, S. Vavrus, M. Vertenstein, D. Bader, W. Collins, J. Hack, J. Kiehl, and S. Marshall, The Community Earth System Model: A Framework for Collaborative Research, *B. Am. Meteorol. Soc.*, **94**, 1339–1360 (2013).

K. Hutter, Theoretical glaciology: material science of ice and the mechanics of glaciers and ice sheets (Springer, 1983).

T. Isaac, G. Stadler, and O. Ghattas, Solution of nonlinear Stokes equations discretized by high-order finite elements on nonconforming and anisotropic meshes, with application to ice sheet dynamics, *submitted for publication and currently available at*: http://arxiv.org/abs/1406.6573.

I. Joughin, B. E. Smith, I. M. Howat, T. Scambos, and T. Moon, Greenland flow variability from ice-sheet-wide velocity mapping, *J. Glaciol.*, **56**, 415–430 (2010).

A. Khazendar, E. Rignot, and E. Larour, Roles of marine ice, rheology, and fracture in the flow and stability of the Brunt/Stancomb-Wills Ice Shelf, *J. Geophys. Res.* **114** (2009), doi:10.1029/2008JF001124.

E. Larour, H. Seroussi, M. Morlighen, and E. Rignot, Continental scale higher order, high spatial resolution, ice sheet modeling using the Ice Sheet System Model (ISSM), *J. Geophys. Res.*, **117**(FO1022), 1–20 (2012).

E. Larour, H. Seroussi, M. Morlighem, and E. Rignot, Continental scale, high order, high spatial resolution, ice sheet modeling using the Ice Sheet System Model (ISSM), *J. Geophys. Res.*, **117**(F01022), 1–20 (2012),

doi:10.1029/2011JF002140.

J.-F. Lemieux, S. Price, K. Evans, D. Knoll, A. Salinger, D. Holland, and A. Payne, Implementation of the Jacobian-free Newton-Krylov method for solving first-order ice sheet momentum balance, *J. Comput. Phys.* **230**, 6531–6545 (2011).

W. Leng, L. Ju, M. Gunzburger, S. Price, and T. Ringler, A Parallel Higher-Order Accurate Finite Element Nonlinear Stokes Ice Sheet Model and Benchmark Experiments, *J. Geophys. Res.*, **117**(F1), 1–24 (2012).

W. Leng, L. Ju, M. Gunzburger, and S. Price, Manufactured solutions and the numerical verification of isothermal, nonlinear, three-dimensional Stokes ice sheet models, *Cryosphere*, **6** 2689–2714 (2012).

W. Leng, L. Ju, M. Gunzburger, and S. Price, A Parallel Computational Model for Three-Dimensional, Thermo-Mechanical Stokes Flow Simulations of Glaciers and Ice Sheets, *Commun. Comput. Phys.*, *in press and currently available at*: http://www.global-sci.com/galley/CiCP-272.pdf.

W. Lipscomb, R. Bindschadler, S. Price, E. Bueler, J. Johnson, and D. Holland, A community ice sheet model for sea level prediction, *Eos. Trans. AGU* **90**(3), 23, (2008).

W. Lipscomb, J. Fyke, M. Vizcaino, W. Sacks, J. Wolfe, M. Vertenstein, A. Craig, E. Kluzek, and D. Lawrence, Implementation and Initial Evaluation of the Glimmer Community Ice Sheet Model in the Community Earth System Model, *J. Climate*, **26**, 7352–7371 (2013) doi:10.1175/JCLI-D-12-00557.1.

C. Little, Toward a new generation of ice sheet models, *Eos. Trans. AGU*, **88**(52) 578–579 (2007).

Los Alamos National Laboratory, Community Ice Sheet Model (CISM), March 2014, URL: http://oceans11.lanl.gov/trac/CISM.

D. Macayeal, Large-Scale Ice Flow Over a Viscous Basal Sediment - Theory and Application to Ice Stream-B, Antarctica, *J. Geophys. Res.*, **94**, 4071–4087 (1989).

D. MacAyeal, V. Rommelaere, P. Huybrechts, C. Hulbe, J. Datemann, and C. Ritz, An ice-shelf model test based on the Ross Ice Shelf, Antarctica, *Ann. Glaciol.*, **23**, 46–51 (1996).

L. Morland, Unconfined ice-shelf flow, *In Dynamics of the West Antarctic Ice Sheet Proc. Workshop held in Utrecht*, May 6–8, 1985 (ed. C. van der Veen and J. Oerlemans), 99–116 (1987).

M. Morlighem, E. Rignot, H. Seroussi, E. Larour, H. Ben Dhia, and D. Aubry, Spatial patterns of basal drag inferred using control methods from a full-Stokes and simpler models for Pine Island Glacier, West Antarctica, *Geophys. Res. Lett.*, **37**(L14502), 1–6 (2010), doi:10.1029/2010GL043853.

J. Nye, The Distribution of Stress and Velocity in Glaciers and Ice-Sheets, *Proc. R. Soc. London, Ser. A*, **239**(1216), 113–133 (1957).

F. Pattyn, A new three-dimensional higher-order thermomechanical ice-sheet model: basic sensitivity, ice stream development, and ice flow across subglacial lakes, *J. Geophys. Res.*, **108**(B8, 2382) 1–15 (2003).

F. Pattyn, L. Perichon, A. Aschwanden, B. Breuer, B. de Smedt, O. Gagliardini, G. Gudmundsson, R. Hindmarsh, A. Hubbard, J. Johnson, T. Kleiner, Y. Konovalov, C. Martin, A. Payne, D. Pollard, S. Price, M. Ruckamp, F. Saito, O. Soucek, S. Sugiyama, and T. Zwinger, Benchmark experiments for higher-order and full-Stokes ice sheet models (ISMIP-HOM), *Cryosphere*, **2**(2), 95–108 (2008).

R. Pawlowski, J. Shadid, J. Simonis, and H. Walker, Globalization techniques for Newton-Krylov methods and applications to the fully coupled solution of the Navier-Stokes equations, *SIAM Rev.*, **48**(4), 700–721 (2006).

R. Pawlowski, E. Phipps, and A. Salinger, Automating embedded analysis capabilities and managing software complexity in multiphysics simulation, Part I: Template-based generic programming, *Sci. Program.*, **20**,

197–219 (2012).

R. Pawlowski, E. Phipps, A. Salinger, S. Owne, C. Siefert, and M. Staten, Automating embedded analysis capabilities and managing software complexity in multiphysics simulation, Part II: Application to partial differential equations, *Sci. Program.*, **20**, 327–345 (2012).

M. Perego, M. Gunzburger, and J. Burkardt, Parallel finite-element implementation for higher-order ice-sheet models, *J. Glaciol.*, **58**(207), 76–88 (2012).

M. Perego, S. Price, and G. Stadler, Optimal Initial Conditions for Coupling Ice Sheet Models to Earth System Models, *J. Geophys. Res.* (2014), *published online and available at:* doi:10.1002/2014JF003181.

N. Petra, J. Martin, G. Stadler, and O. Ghattas, A computational framework for infinite-dimensional Bayesian inverse problems: Part II. Stochastic Newton MCMC with application to ice sheet inverse problems, *SIAM J. Sci. Comput.*, *in press and currently available at:* http://arxiv.org/abs/1308.6221.

E. Phipps, and R. Pawlowski, Efficient Expression Templates for Operator Overloading-based Automatic Differentiation, in *Recent Advances in Algorithmic Differentiation*, eds. S. Forth, P. Hovland, E. Phipps, J. Utke, and A. Walther (Springer, 2012).

D. Pollard, and R. Deconto, Modelling West Antarctic ice sheet growth and collapse through the past five million years, *Nature*, **458**, 329–332 (2009), doi:10.1038/nature07809.

S. Price, E. Waddington, and H. Conway, A full-stress, thermomechanical flow band model using the finite volume method, *J. Geophys. Res.* **112**(F03020), 1–17 (2007).

V. Rommelaere, Ice Shelf Models Intercomparison: setup of the experiments, unpublished document, 1996, URL: http://homepages.vub.ac.be/~phuybrec/eismint/shelf-descr.pdf.

I. Rutt, M. Hagdorn, N. Hulton, and A. Payne, The Glimmer community ice sheet model, *J. Geophys. Res.*, **114**(F02004), 1–22 (2009).

A. Salinger, E. Burroughs, R. Pawlowski, E. Phipps, and L. Romero, Bifurcation tracking algorithms and software for large scale applications, *Int. J. Bifurcat. Chaos*, **3**(15), 1015–1032 (2005).

A. Salinger, E. Phipps, G. Hansen, I. Kalashnikova, J. Ostien, W. Sun, Q. Chen, A. Mota, R.Muller, E. Nielsen, and X. Gao, Albany: A Component-Based Partial Differential Equation Code Built on Trilinos, *in preparation for submission*.

S. Schaffer, A semicoarsening multigrid method for elliptic partial differential equations with highly discontinuous and anisotropic coefficients, *SIAM J. Sci. Comput.*, **20**(1), 228–242 (1998).

C. Schoof, Coulomb friction and other sliding laws in a higher-order glacier flow model, *Math. Mod. Meth. Appl. S.*, **20**(1), 157–189 (2010).

C. Schoof, and R. Hindmarsh, Thin-Film Flows with Wall Slip: An Asymptotic Analysis of Higher Order Glacier Flow Models, *Q. J. Mech. Appl. Math.*, **63**, 73–114 (2010).

H. Seroussi, H. Ben Dhia, M. Morlighem, E. Larour, E. Rignot, and D. Aubry, Coupling ice flow models of varying orders of complexity with the Tiling method, *J. Glaciol.*, **58**, 776–786 (2012), doi:10.3189/2012JoG11J195.

S. Shannon, A. Payne, I. Bartholomew, M. van der Broeke, T. Edwards, X. Fettweis, O. Gagliardini, F. Gillet-Chaulet, H. Goelzer, M. Hoffman, P. Huybrechts, D. Mair, P. Nienow, M. Perego, S. Price, P. Smeets, A. Sole, R. van de Wal, and T. Zwinger, Enhanced basal lubrication and the contribution of the Greenland ice sheet to future sea-level rise, *Proc. Natl. Acad. Sci. USA*, **110**, 14156–14161 (2013), doi:10.1073/pnas.1212647110.

J. Shewchuk, Triangle: Engineering a 2D Quality Mesh Generator and Delaunay Triangulator, in *Applied Computational Geometry: Towards Geometric Engineering*, **1148**, *Lecture Notes in Compute Science*, 203–222 (Springer-Verlag, 1996).

S. Solomon, D. Qin, M. Manning, Z. Chen, M. Marquis, K. Averyt, M. Tignor, and H. Miller, Climate change 2007: The physical science basis. *Contribution of Working Group I to the Fourth Assessment Report of the Intergovernmental Panel on Climate Change* (Cambridge Univ Press, Cambridge, UK, 2007).

W. Strang, and G. Fix, Analysis of the finite element method, (Prentice-Hall series in automatic computation, 1973).

W. Sun, J. Ostien, and A. Salinger, A stabilized assumed deformation gradient finite element formulation for strongly coupled poromechanical simulations at finite strain, *Int. J. Numer. Anal. Met.*, **37**(16), 2755–2788 (2013).

R. Tuminaro, ML's SemiCoarsening Feature, *Addition to ML 5.0 Smoothed Aggregation User's Guide, Sandia National Laboratories Report, SAND2006-2649*, Sandia National Laboratories, Albuquerque, NM (2014).

University Corporation for Atmospheric Research (UCAR), CESM 1.0: Community Earth System Model, 2013, URL: http://www.cesm.ucar.edu/models/cesm1.0.

C. van der Veen, and ISMASS (Ice Sheet Mass Balance and Sea Level) Working Group, Ice Sheet Mass Balance and Sea Level: A Science Plan, *Scientific Committee on Antarctic Research (SCAR) Report No. 38*, ISSN 1755–9030 (2010).